Aerospace Science and Technology 155 (2024) 109740

Contents lists available at ScienceDirect

Aerospace Science and Technology

journal homepage: www.elsevier.com/locate/aescte

Aerodynamic and aeroacoustics investigation of tandem propellers in hover for eVTOL configurations

Daniele Granata, Alberto Savino, Donato Grassi, Luca Riccobene, Alex Zanotti *

Politecnico di Milano, Dipartimento di Scienze e Tecnologie Aerospaziali, via La Masa 34, 20156, Milan, Italy

ARTICLE INFO

Communicated by Antonio Filippone

Keywords:
Aerodynamics
Aeroacoustics
Particle image velocimetry
Vortex particle method
eVTOL

ABSTRACT

The present study investigates the aerodynamic interactions and the aeroacoustic footprint of a tandem propellers configuration typical of a multi-rotor eVTOL aircraft in hover conditions. In particular, an experimental campaign was conducted to collect a comprehensive aerodynamic and aeroacoustic database over two scaled propellers models in tandem. Aerodynamic loads and acoustic measurements were performed in an anechoic test chamber. Measurements also included flow field surveys using stereoscopic PIV technique. The configurations tested included twin propellers in side-by-side and staggered configurations with partial overlap between rotor disks. The activity was completed by numerical simulations performed with the mid-fidelity aerodynamic solver DUST. The analysis of experimental and numerical results enabled to provide a robust comprehension of the different flow mechanisms that characterise aerodynamic interaction between propellers wakes by changing longitudinal and lateral distances as well as blades sense of rotation. In particular, the effects of these interactions on both the aerodynamic performance and aeroacoustic footprint was investigated. Specifically, the partial overlap between propellers disks leads to a conspicuous reduction of aerodynamic performance of the propeller invested by front propeller slipstream as well as an increase of the acoustic emission of the dual propeller system.

Notation

BPF	Blade Passage Frequency [Hz]
CFD	Computational Fluid Dynamics
c_n	blade sectional normal force coefficient
C_P	power coefficient, $= P/(\rho n^3 D^5)$
C_T	thrust coefficient $= T/(\rho n^2 D^4)$
D	propeller diameter [m]
eVTOL	electrical Vertical Take Off and Landing aircraft
L_x	longitudinal distance between the propeller disks
L_y	lateral distance between the propeller axis
M	Mach number
n	rotational speed [rad/s]
OASPL	Overall Averaged Sound Pressure Level [dB]
P	propeller power [W]
Q_{crit}	Q-criterion
R	propeller blade radius [m]
SPL	Sound Pressure Level [dB]
T	propeller thrust [N]
u	axial velocity component [m/s]
UAM	Urban Air Mobility
VPM	Vortex Particle Method
V_∞	wind tunnel freestream velocity [m/s]
$x-y-z$	reference system
Z-Vorticity	out-of-plane vorticity component [1/s]
α	sectional propellers blades angle of attack [deg]
β	blade pitch angle at 75%R [deg]
Δ	variation with respect to single propeller
ϕ	blade azimuthal angle [deg]
ρ	air density [kg/m^3]
θ	angular position of the microphones [deg]

Subscripts:

0	single propeller

1. Introduction

Urban traffic of VTOL aircraft is expected to grow rapidly in next years. Indeed, there has been an increasing interest in developing a novel short-range personal aviation concept as an efficient and sustainable alternative to ground transportation in densely populated urban

* Corresponding author.
E-mail address: Alex.Zanotti@polimi.it (A. Zanotti).

https://doi.org/10.1016/j.ast.2024.109740
Received 30 July 2024; Received in revised form 11 November 2024; Accepted 12 November 2024
Available online 16 November 2024

areas. These aircraft, characterised by the capability of vertical take-off and landing and utilising electric distributed propulsion (eVTOLs), are benefiting from advancements in various technological areas such as electric motors and batteries [1]. However, these innovative architectures present unprecedented challenges due to their unique design, particularly characterised by using several rotors/propellers. Therefore, ensuring safety, reliability and noise reduction are key aspects that must be thoroughly addressed to gain regulatory approval and public acceptance.

Among the most promising eVTOL configurations, the multi-rotor drone-like configuration combines the characteristics of a traditional helicopter and a drone. On the other hand, tiltrotors architectures, subjects of ongoing research towards achieving mature technology [2] [3] [4] [5], inspired the eVTOL vectored-thrust concept. Both these configurations, being at the forefront of aerospace technology, should be still object of research studies that comprehensively addresses and resolves engineering challenges and provides methods to facilitate their transition into mature technology.

As previously stated, mission and safety requirements of such eVTOLs drive the vehicle design towards the use multi-rotor and/or multi-wing architectures [6]. The aerodynamics of these new concepts is generally dominated by complicated rotors-wing-airframe interactions that still represent complex challenges to be accurately investigated [7,8]. The profound impact of these interaction mechanisms on the aircraft's aerodynamic performance and noise generation emphasizes the crucial need for their investigation. Understanding these complexities is of utmost importance to gain a comprehensive understanding of the complex environment surrounding eVTOL vehicles. Research efforts has already been started in recent years with the development of aerodynamic mid-fidelity tools [9–12] based on vortex particle method (VPM) which offer an optimal trade-off between computational cost and desired accuracy, particularly in the preliminary stages of the design, as they allow the engineers to investigate the behaviour of the vehicles by taking into consideration complex aerodynamic interactions otherwise difficult to account for classical high-fidelity CFD tools [13].

Investigation to understand noise pollution produced by a rotary-wing aircraft has used various different ways of testing, both experimental and numerical. Full size tests are not always possible and could require a very high effort. Thus, the use of scaled models in anechoic chambers or wind tunnels under monitored and controlled conditions can be considered a valuable tool also for validation of numerical simulation software. Indeed, recent literature shows a great number of experimental and numerical works aimed at investigating aeroacoustics of multi-rotor concepts. For instance, Jia and Lee [14] investigate the acoustics of a quadrotor eVTOL using a high-fidelity simulation tool, founding that no rotor-to-rotor interaction can be identified due to a vertical separation distance between the front and rear rotors and that the eVTOL fuselage does not have significant impact on acoustics, while both rotor aerodynamics and acoustics can be greatly influenced as the rotor size increases. Zarri et al. [15] investigated the root mechanisms causing tonal noise in a multicopter drone configuration by an hybrid numerical methodology coupling unsteady Reynolds-Averaged Navier-Stokes simulations with a computational aeroacoustic approach based on the Finite Element Method. This approach, validated by comparing the predicted tones with existing acoustic measurements, enabled to quantify propeller-propeller and propeller-airframe aerodynamic installation effects as well as airframe scattering effects. Another numerical study focused on a full multi-rotor vehicle configuration was performed by Sagaga and Lee [16]. This work investigated, in particular, the effect of rotor overlap and fuselage on aerodynamic performance and noise of a side-by-side rotor aircraft in hover. Simulations results show a substantial influence of the fuselage on rotor performance related to an improvement of figure of merit and a considerable increase of noise levels due to the absence of rotor overlap.

A particular effort was spent in recent years on the investigation of the effects on noise of basic aerodynamic interaction mechanisms between side-by-side propellers. Thai et al. [17] investigated the interactions of small hovering rotors using both simulations and experimental analysis conducted in an anechoic chamber. In particular, a dual rotor interaction was analysed by reproducing a pair of co-rotating rotors and a pair of counter-rotating rotors positioned at different separation distance. Poggi et al. [18] present a numerical investigation of noise radiated by two side-by-side propellers showing that blade tip Mach number strongly affects the magnitude and directivity of the radiated noise, while increasing the tip-clearance produces an increase of the spatial frequency of the noise directivity for both co-rotating and counter-rotating configurations. The work by Afari and Mankbadi [19] describes results of a high-fidelity simulation using Hybrid LES-Unsteady RANS approach coupled with far-field sound predictions performed using Ffowcs-Williams-Hawkings formulation of two side-by-side counter-rotating propellers in hover and in forward flight conditions. The comparison with results obtained with the single propeller configuration enabled to identify the aerodynamic changes resulting from the proximity of the two propellers and to understand the mechanisms causing the changes in the radiated sound. Moreover, Alvarez et al. [20] explored the use of a classical URANS solver and of a meshless Lagrangian solver based on VPM both coupled with an aeroacoustics solver for tonal and broadband noise predictions to investigate the acoustic noise caused by aerodynamic interactions of a dual propellers system in hover. Simulations results showed no sensitivity of noise to blade loading distribution changes obtained by changing the lateral distance in side-by-side configuration, while noise can be mitigated by spacing the rotors in the downstream direction with an optimal spacing being about half a diameter.

Now citing experimental activities in this field of investigation, Celik et al. [21] performed an extensive wind tunnel campaign aimed at evaluating the effect of the separation distance between two side-by-side rotors on the noise directivity patterns, spectral characteristics and temporal features of the radiated noise in both hovering and edge-wise flight conditions. Overall sound pressure level measurements showed a dependence on the separation distance and advance ratio, while spectral characteristics elucidate the influence of separation distance on tonal and broadband energy content. Moreover, Nargi et al. [22] conducted an experimental investigation of twin co-rotating rotors aimed to evaluate interactional effects on aerodynamic performance, flow fields and acoustic emissions in hover due to the relative change of lateral distance between side-by-side disks.

Particular attention was also devoted in the recent literature on the experimental study of multi-propellers system equipped with a wing, thus resembling the most promising eVTOL aircraft architectures under investigation. In particular, Zawodny et al. [23] performed a series of aerodynamic performance and acoustic measurements on a range of inboard propeller-wing interaction configurations obtained by changing the axial and vertical positioning of the wing relative to the propeller slipstream under a constant propeller advance ratio. Moreover, Goldschmidt et al. [24] performed an experimental investigation of the noise and forces generated by tandem eVTOL rotors in forward flight. Noise results showed that the overall noise levels were dominated by the noise at the rear (lift) rotor blade pass frequency, having maximum levels on the retreating side of the rotors, while adding a wing and a boom favorably altered the unsteady loading noise source of the lift rotor and decreased the overall noise levels. In addition, Monteiro et al. [25] recently investigated by wind tunnel tests the acoustic characteristics of a distributed propeller-wing system in a tractor configuration, focusing on the potential for noise reduction using the synchrophasing technique, i.e. varying relative blade-phase angles. Experimental results indicated a certain blade-phase angle that could provide the quietest noise levels for the investigated three adjacent propellers with nacelles mounted side-by-side on the leading edge of a wing and further considered an enhanced reduction of noise by increasing wing angle of attack.

Recently, a great effort in the study of aerodynamics performance and noise footprint related to multi-rotor configurations has been pro-

viding by the activities conducted in the GARTEUR Action Group HC/AG-26 [26]. The collaborative work of this group of research partners was aimed at providing a comprehensive experimental database focused on propeller-propeller interaction for the validation of numerical solvers with different level of fidelity. As partner of this consortium, Politecnico di Milano (POLIMI) contributed to the activities of this Action Group by performing a comprehensive experimental campaign on a test case consisting by two scaled propellers models with open geometry. Indeed, POLIMI has been at the forefront of multiple experimental campaigns and numerical activities aimed at investigating interactional aerodynamics phenomena in complex eVTOL configurations. Several past activities were aimed to provide a comprehensive understanding related to a dual propeller configuration in the different flight conditions that characterise eVTOL mission, from cruise [27] to transition maneuver [28]. Moreover, wing-propeller configuration was also deeply investigated by means of both experiments [29] and mid-fidelity numerical simulations [30]. In this framework, the present article is aimed to close the loop of the investigated flight conditions by performing experiments of this dual propeller system in hover. The goal of the activity was to provide a completely open experimental database for numerical solvers validation as well as to comprehend the effects of aerodynamics interaction between the propellers on both aerodynamic performance and acoustic footprint. A comprehensive set of configurations was tested including both side-by-side propellers and tandem propellers with a partial overlap between the propellers disks at different longitudinal distances. In particular, the investigation of staggered tandem configurations represents the main novelty proposed by the present work with respect to recent literature. The tests enabled to evaluate quantitatively the effects on aeroacoustics due to interacting aerodynamics phenomena. Load measurements results were also correlated to acoustic noise emission. Furthermore, stereoscopic PIV measurements were performed in a dedicated campaign to investigate interactional flow fields, particularly in the propellers wake. The test campaign provided a comprehensive database over an open geometry including both aerodynamic and aeroacoustic results.

In addition to experimental activity, numerical simulations performed with the mid-fidelity solver DUST [31] reproducing some selected wind tunnel test configurations enabled to provide insights useful to enhance the physical comprehension of the interactional mechanisms for some selected test conditions characterised by a higher degree of complexity of flow interaction. Indeed, numerical simulations were performed to investigate the effects of partial overlap between propeller disks in staggered configuration with different sense of rotation of propellers blades.

2. Experimental set up

2.1. Acoustic and load measurements set up

The experimental activity was performed at Politecnico di Milano in the $4m$ x $4m$ x $4m$ anechoic chamber of PoliMi Sound and Vibration Laboratory (PSVL). The test chamber have a 150 Hz cut-off frequency. Two three-bladed propeller models were used for the test campaign. The models are the same used for the previous activities described in [27,28]. The propeller was designed using a three-bladed hub equipped with VarioProp 12C blades, thus resulting in a propeller disk diameter D equal to 300 mm. An internal aluminium frame was designed to support the propeller driving system and a bi-axial strain gauge load cell Futek MBA500 (range ±50 lbs for thrust and of ±50 lbs-in for torque, non-linearity ±0.25% Rated Output, non-repeatability ±0.05% Rated Output). The propeller was driven by a Scorpion brushless motor (5.3 kW continuous power) with shaft connected directly to propeller hub. The motor was powered by an external PWM-controlled electronic speed controller. A custom software developed in Labview was used to keep controlled both propellers at the desired rotational speed. A maximum fluctuation below 1% of the target rotational speed of the propellers was found during the tests. The blade azimuth phase of the two propellers blades during the tests were not synchronised. Indeed, the accurate control of propellers blade phase angles at the high RPM selected for the tests was not feasible due to hardware limitation of the hobby-grade external speed controller available for the tests. The propeller models were mounted on a metallic frame made by 30 mm × 30 mm squared section aluminium struts. The metallic frame was completely shielded with sound absorbing material. A picture of the tests set up is shown in Fig. 1(a). The aluminium strut used to support the propellers, acting as a rail, enabled to manually modify the lateral separation distance between the propellers models axis of rotation (L_y) in side-by-side configuration, i.e. with propellers disks lying on the same plane. Moreover, the metallic frame allowed to change also the longitudinal distance (L_x) between the propellers disks, thus enabling a tandem configuration with overlapping of the propellers disks. Acoustic measurements were made by an array of twelve ROGA MI19 1/4" IEPE microphones (Frequency response 20 Hz – 20 kHz, Sensitivity 50 mV/Pa, Uncertainty 0.2 dB) positioned at 12 propeller disk radii (R) from the center of the test horizontal section. Fig. 1(b) shows a sketch of the propellers in the anechoic test chamber, the microphones positions highlighted as circular dots as well as their azimuthal angular position θ. For each test run, loads and microphones signals were acquired for 10 seconds at an acquisition frequency of 25.6 kHz. Both loads and microphones measurements were repeated over four runs for each test conditions and results obtained from the four acquisitions were averaged. Load cell and microphones signals acquisition started 10 seconds after that both propellers have reached an accurate steady state target RPM level. Thus, a proper quantification of flow recirculation effects in the anechoic test chamber as done in Weitsman et al. [32] and Stephenson et al. [33] could not be feasible from the present measurements that were focused to provide a comparative study between different tandem propellers configurations. On the other hand, a quantification of the recirculation effects for the present activity could be provided by analogy with the outcomes of these recent literature works [32,33]. Indeed, according to these works, by using a test set up that almost reproduce the same dimensions of propeller diameter with respect to anechoic test chamber volume, mean loads measurements as well as the first fundamental harmonic of the BPF are relatively unaffected by the flow recirculation within the room, while after flow recirculation is formed, the amplitudes of higher BPF harmonics can be increased in excess up to 15 dB.

Fig. 2 shows the reference frame and notation to define the propellers layout during the tests that will be also used to present the results in Sec. 4. Propeller 1 (right one in Fig. 2(a)) was considered as the reference propeller to evaluate the effect of the aerodynamic interaction provided by the influence of the slipstream of propeller 2. Moreover, the definition of propeller blade azimuthal angle is illustrated in Fig. 2(b).

2.2. PIV measurements

The flow field around both the single and tandem propeller configurations is investigated by means of stereo Particle Image Velocimetry (sPIV) technique. Measurements were performed in a dedicated test campaign in a separate room with similar dimensions to avoid pollution and to follow safety rules of the anechoic test chamber.

A picture of the sPIV setup is shown in Fig. 3. Two double-shutter ILA.PIV.sCMOS cameras with a 16 bit 2560×2160 pixels array equipped with Canon© 28mm lens were arranged in angular Scheimpflug configuration, in order to make possible the reconstruction of the three-component displacement vector in the plane of the light sheet. During the experiment, the air flow was seeded with 1-2 μm oil droplets generated by a particle generator PIVpart30 by PIVTEC equipped with Laskin atomizer nozzles. Illumination was provided by a Quantel Evergreen Nd:Yag double-pulse laser with an output energy of 200 mJ and wavelength of 532 nm. In order to enlighten the area of interest on midspan plane between the two propellers, a 90° mirror was applied to the optics of the laser positioned on the floor. A general in-situ calibration

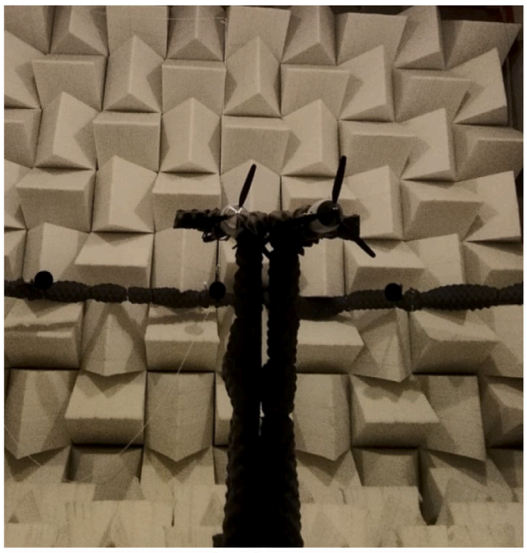

(a)

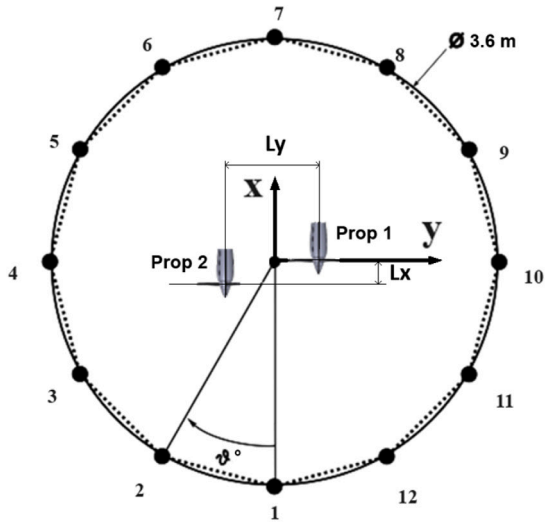

(b)

Fig. 1. (a) Experimental set up in the Politecnico di Milano Sound and Vibration Laboratory (PSVL) anechoic chamber; (b) Sketch of the propeller models test set up, microphones positions highlighted as circular dots.

procedure was conducted to obtain the mapping functions between the image planes and object planes for the sPIV measurements, resulting in a magnification factor of 5 pixel/mm. Image pairs analysis was performed using PIVview 3C software developed by PIVTEC. The instantaneous velocity fields were obtained using a frame-to-frame multigrid cross-correlation technique using an interrogation window starting from 128 pixels × 128 pixels to 32 pixels × 32 pixels. An effective overlap of 50% of the interrogation windows was considered in PIV image pairs post-processing, thus resulting in a spatial resolution of about 3 mm between adjacent measurement points. Laser frequency was kept at 15 Hz for both free-run and phase-locked acquisitions. Image pairs that contained shadows due to the impingement of the laser sheet on blades were discarded from the post-processing. Stereo PIV surveys were performed for a selected number of test configurations with respect to the ones considered for loads measurements. In particular, free-run 3C PIV measurements were performed to obtain a total number of 500 image pairs to calculate the ensemble averaged flow fields. On the other hand, phase-locked 3C PIV measurements triggered on different propeller 1 blade azimuth position (see Fig. 2(b)) were performed by capturing 1000 image pairs for each blade azimuthal angle ϕ. Even if the two propellers were not synchronised in phase during the tests, the use of markers positioned on propeller 2 spinner and nacelle enabled to optically select the image pairs from the collected overall database where both the propellers have the same azimuthal angular position of the blades. By considering an acceptable deviation of $\pm 2°$ for propeller 2 blade azimuthal angle, this technique enabled to calculate phase-averaged flow fields at same blade azimuth for both propellers by selecting a number of image pairs ranging from 75 to 100, depending on the test configuration.

Table 1
Test parameters of the investigated configurations.

Configuration	RPM	β at 75%R	Sense of Rotation	L_x/R	L_y/R
Single Prop	9000	15°	-	-	-
Tandem Props	9000	15°	Co-rot	0	[2.1 - 3]
Tandem Props	9000	15°	Co-rot	0.5	[1.5 - 3]
Tandem Props	9000	15°	Counter-rot	0.5	[1.5 - 3]
Tandem Props	9000	15°	Co-rot	1	[1.5 - 3]

2.3. Test conditions

Table 1 presents the test parameters of the propellers configurations discussed in the present work.

Test conditions consisted of runs performed with rotational speed of both propellers controlled to 9000 RPM. The collective pitch of both the propellers blades was fixed to $\beta = 15°$. Tests included side-by-side configurations with co-rotating propellers lying on the same plane ($L_x/R = 0$) at different lateral distances L_y. In particular, the minimum lateral distance of $L_x/R = 2.1$ was considered for safety during the tests. Moreover, staggered propeller configurations were tested with two different longitudinal distance between the disks, i.e. $L_x/R = 0.5, 1$. For staggered configurations the lateral distance was changed in the range between $L_y/R = 1.5$ and $L_y/R = 3$. Moreover, staggered configurations tests with $L_y/R < 2$ reproduce a partial overlap between the propellers disks. For test configurations with $L_x/R = 0.5$ also the effect of blades sense of rotation was investigated.

3. Numerical simulations

Numerical simulations were performed using the mid-fidelity aerodynamic solver DUST, developed by Politecnico di Milano [31], to provide insights useful to enhance the physical comprehension of the interactional mechanisms occurring in hover conditions for some selected test conditions. DUST is a VPM-based [34] solver implementing several numerical elements as lifting lines, surface panels and non-linear vortex lattices. The reader is referred to [31] for a complete description of the mathematical formulation of the code. The code was thoroughly validated against experiments and high fidelity CFD for eVTOL configurations [9,35]. In the present work DUST numerical model of the propeller is the same used in the recent investigation of tandem propellers interaction [28], thus the reader is referred to these works for details on the open geometry of the propeller to be used to reproduce the test conditions. The complete geometry of the propeller will be provided on request to authors. In particular, an amount of 50 lifting lines in the spanwise direction were used to model each blade, while spinner-nacelle surface was modelled using 1212 surface panels. The selection of the spatial and time-step discretisation parameters used for the simulations was dictated by a spatial and time-dependence study reported in [36] for the sake of consistency. The propeller mesh built for DUST simulations is shown in Fig. 4.

DUST simulations reproduced isolated and some selected tandem propellers configurations, as tested during the experiments. For tandem propeller configurations, simulations were performed with propellers blades synchronised in terms of azimuthal angle, in co-rotating

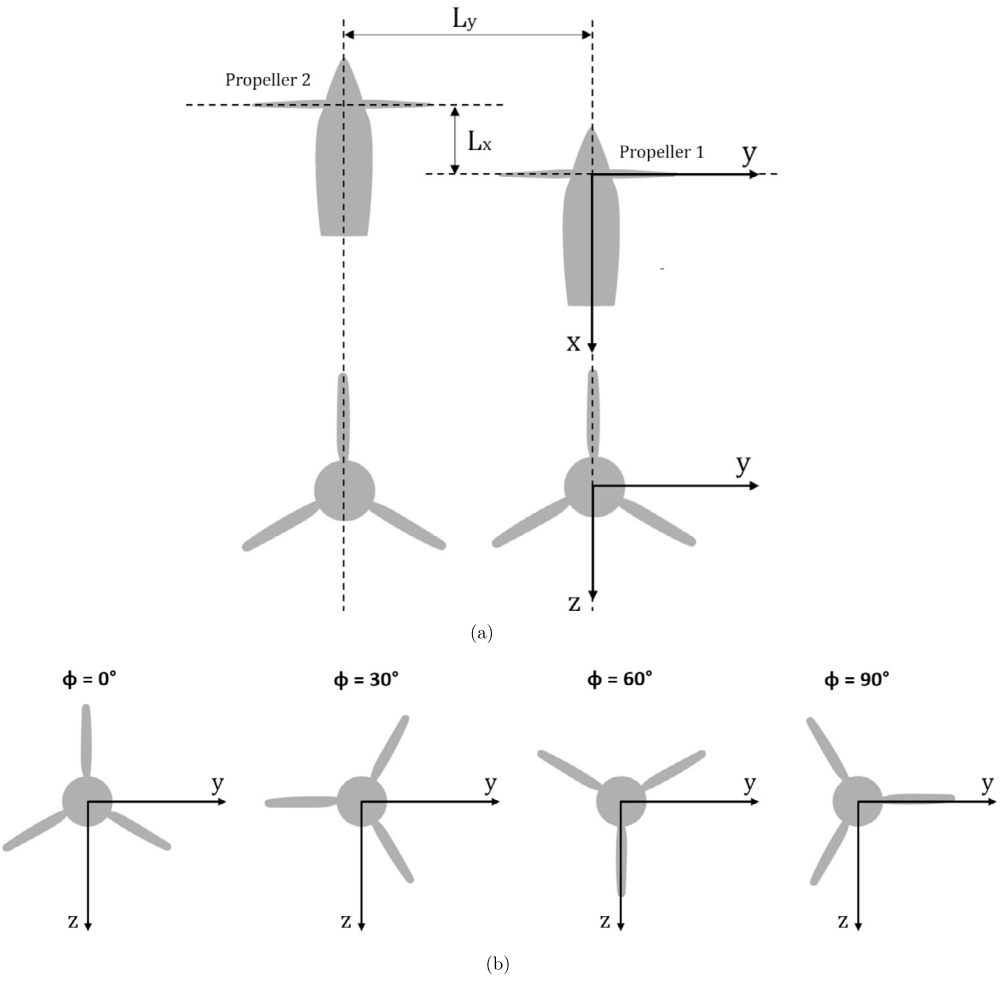

Fig. 2. (a) Tandem propeller reference frame; (b) Propeller blade azimuthal angle definition.

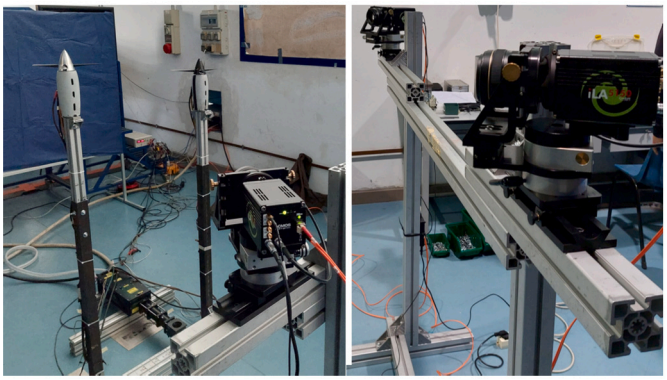

Fig. 3. Stereoscopic PIV experimental setup.

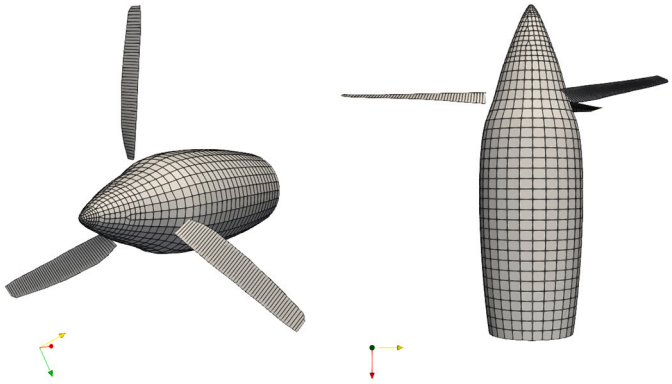

Fig. 4. Propeller mesh used for DUST simulations.

or counter rotating configuration. Concerning the total simulation time, effectively expressed by the number of overall propeller revolutions performed, this parameter was fixed to obtain whether an approximately steady state condition of the computed loads in case of single propeller configuration or a fully periodic oscillation of the rear propeller loads after the impingement of the wake released by the front one for the tandem interacting test cases. The integral loads acting on the propellers were averaged over the last computed three propellers revolutions. Simulations of the single and tandem propeller configurations were performed considering respectively a length of 10 and 15 propeller revolutions both with a time discretization of 5° blade azimuthal angle. The computational time required to complete a simulation was about 1h and 2h respectively for the single and tandem propellers configurations, by using a workstation with a Dual Intel® Xeon Gold 6230R @2.10GHz processor with 52 physical cores and 2 threads for each core.

4. Results and discussion

4.1. Aerodynamic performance and flow field analysis

In the present section, the experimental results obtained from aerodynamic loads and sPIV measurements in hover conditions are firstly shown and discussed. Aerodynamic performance results discussion will be enhanced by the use of numerical simulations results to improve the

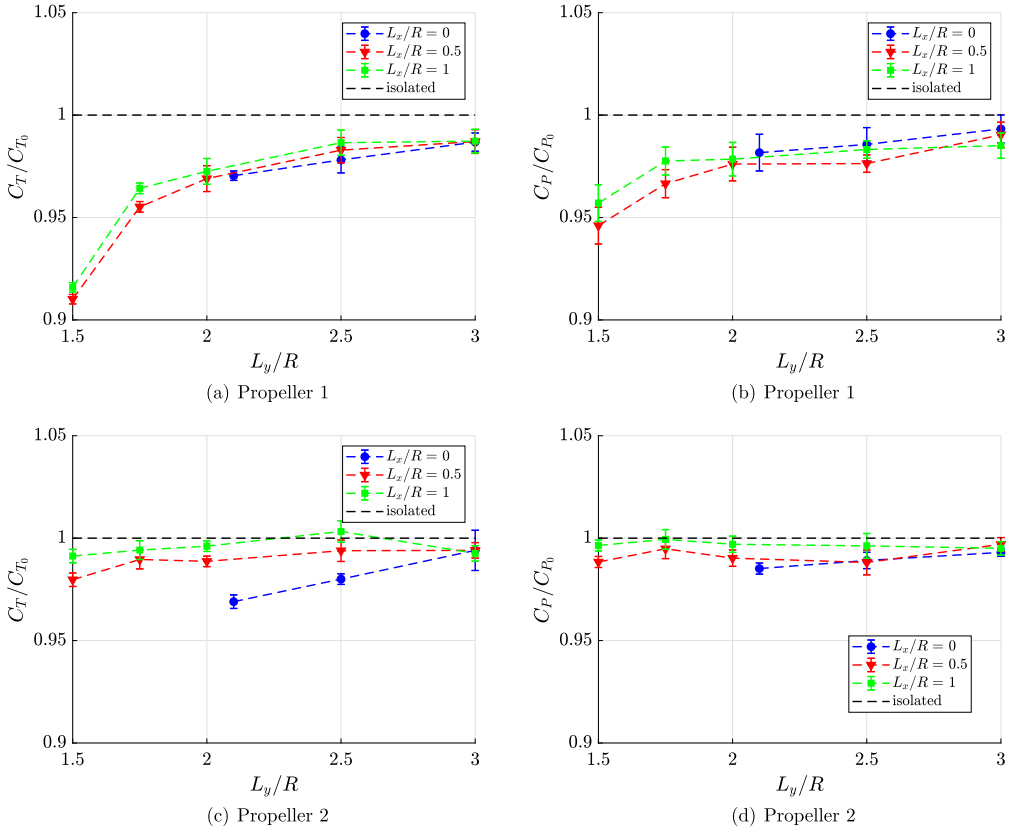

Fig. 5. Comparison of thrust and power coefficients measured for the two propellers in side-by-side and tandem staggered configurations with respect to longitudinal (L_x) and lateral distances (L_y).

physical comprehension of the interactional flow features and their effects on propeller loading.

4.1.1. Loads measurements results

Aerodynamic loads results are shown in terms of thrust and power coefficients measured for both propellers. Both aerodynamics coefficients are presented divided by the values measured for the single propeller test case. The curves show error bars related to standard deviation of the repeated loads measurements over four runs. Fig. 5 shows the behaviour of the aerodynamic coefficients measured for both propellers with respect to the lateral separation L_y for different values of longitudinal distance L_x. When L_y decreased there is an almost linear decrease of the propeller 1 loads caused by aerodynamic induction effects between the blades of the rotors (see Figs. 5(a) and 5(b)). This behaviour is quite apparent also for the load coefficients measured by propeller 2 in side-by-side configuration, i.e. $L_x/R = 0$ (see Figs. 5(c) and 5(d)). In the lateral separation range when propellers disks are not overlapped, the loads losses are limited and achieve values within the 3% and 2% of the single propeller configuration, respectively for the thrust and power coefficient. This linear decrease of performance is not observed for propeller 2 in the staggered configurations, i.e. $L_x/R = 0.5, 1$. Indeed, for these test cases propeller 2 performance is scarcely influenced by propeller 1 in the whole investigated range of lateral distance. As can be observed in Figs. 5(c) and 5(d), the loads curves measured for propeller 2 almost approach the value measured for the single propeller configuration, particularly by increasing the longitudinal distance, i.e. $L_x/R = 1$.

A more significant load reduction occurs for propeller 1 in the staggered propellers configurations when there is a partial overlapping of the propeller disks. For $L_y/R = 1.75$ the disks are geometrically slightly overlapped but the performance losses are still limited. On the other hand, for $L_y/R = 1.5$, an exponential decrease of propeller 1 loads occurs particularly for thrust coefficient (up to a 10% reduction with respect to single propeller), as the partial overlapping of propellers disks leads to increase the interactional aerodynamic phenomena due to front propeller slipstream impingement on rear propeller.

Fig. 6 shows the comparison of loads measurements results obtained with the co-rotating and counter-rotating blades for the longitudinal separation $L_x/R = 0.5$ and varying lateral separation L_y/R. The trend followed by the aerodynamic loads curves measured with counter-rotating propellers is similar to that observed for co-rotating blades. It is interesting to note that in the range of lateral distance $1.75 < L_y/R < 3$, both thrust and power losses of propeller 1 are lower for the counter-rotating configuration (see Figs. 6(a) and 6(b)). This trend is not observed for propeller 2, where loads curves measured for co- and counter-rotating blades almost resembles the same values (see Figs. 6(c) and 6(d)). Indeed, as for staggered configuration propeller 2 is slightly influenced by propeller 1, blades sense of rotation does not alter propeller aerodynamic performance. On the other hand, focusing now the attention on results measured for propeller 1 at $L_y/R = 1.5$, characterised by the higher degree of aerodynamic interaction due to a conspicuous amount of front propeller slipstream investing the rear propeller, the counter-rotating propeller shows a slightly higher decrease of performance with respect to the co-rotating test case for both thrust and power coefficients (see Figs. 6(a) and 6(b)). This latter behaviour observed on rear propeller performance by changing the blades sense of rotation is explained in details for the overlapped disks test case by comparing the flow physics exposed by DUST simulations results discussed in Subsec. 4.1.3.

4.1.2. PIV measurements results

Flow field analysis started from the comparison of the single propeller configuration with the side-by-side configuration characterised by the minimum lateral distance tested $L_y/R = 2.1$. In particular, ensemble-averaged contours of the longitudinal velocity component u

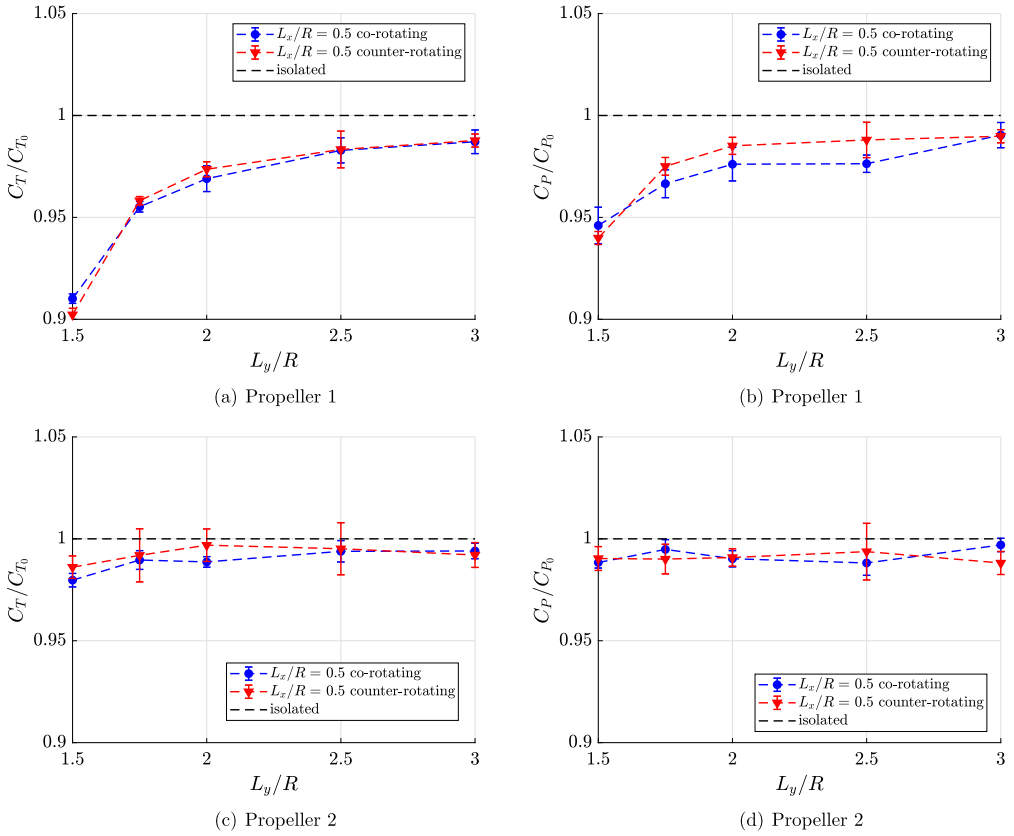

(a) Propeller 1 (b) Propeller 1

(c) Propeller 2 (d) Propeller 2

Fig. 6. Comparison of thrust and power coefficients measured for the two propellers in tandem staggered configurations at longitudinal distance $L_x/R = 0.5$ with respect to blades sense of rotation.

and of the vorticity magnitude calculated using the three velocity components measured by PIV are shown in Fig. 7 to point out the interactional effects provided on propeller 1. The longitudinal velocity component field represented in Fig. 7(a) shows the classical flow topology of a stationary single propeller in hover characterised by a low-speed inflow, distributed almost uniformly along the blade span, and an outflow with the shape of a contracted jet. The averaged velocity component u field evaluated for the side-by-side configuration illustrated in Fig. 7(b) shows a slight reduction of the propeller 1 slipstream contraction with respect to the single propeller. This may be caused by the Coanda effect, as also reported in a similar literature work [37], which tends to pull the wakes of the neighbouring propellers towards each other. The tendency of the blade vortices path to converge is also evident when comparing the averaged vorticity fields in Figs. 7(c) and 7(d). In particular, this representation highlights that the vortices interaction provides a reduction of the vorticity magnitude downstream the propeller disks for the side-by-side test case. As a matter of fact, the modification of the flow field for the side-by-side configuration is quite limited with respect to single propeller, thus supporting the negligible effects observed on propeller loading showing variation of few percents of both thrust and power coefficients. These outcomes are aligned with the main findings of a recent literature work employing a similar test rig [37].

Flow field analysis is now focused on the tandem staggered propellers configurations with longitudinal distance $L_x = 0.5$. In particular, the effects of lateral distance including propellers disks overlap and of blades sense of rotation is illustrated. These aspects represent the main novel contributions of the present work with respect to recent literature as these are rather novel investigated configurations for hover flight conditions. For the sake of consistency, flow field analysis of propellers configurations with $L_x = 1$ are not reported as very slight differences were observed on flow topology with respect to the test cases analysed for lower longitudinal distance.

Fig. 8 shows the comparison of the ensemble-averaged longitudinal velocity component fields for the $L_x = 0.5$ staggered configurations with both co-rotating and counter-rotating propellers. Considering the co-rotating test cases without disk overlapping, i.e. $L_y/R = 2$ and $L_y/R = 2.5$, similarly to what observed for the side-by-side test case shown in Fig. 7(b), a mutual induction, which leads to a dragging effect of the propellers wakes towards each other is still visible. In particular, the maximum induction between the outflows occurs in the aligned-tip configuration $L_y/R = 2$, causing the outflows of the wakes to tend towards each other and altering the classical contracted jet shape observed for the single propeller (see Fig. 7(a)). Once again, the modification of the flow field observed for the test cases without disks overlapping is quite limited with respect to single propeller, thus supporting the negligible effects observed on propeller loading.

On the other hand, at $L_y/R = 1.5$, as the propellers disks partially overlap, the interaction of the slipstreams results in a highly accelerated flow. Indeed, an increase of the magnitude of the longitudinal velocity component of about 15% is observed for the co-rotating test case with respect to single propeller (see Fig. 8(e)). In this case, the increase of the axial velocity investing the propeller disk provides a local decrease of the effective angle of attack experienced by the portion of the blades invested by the front propeller slipstream, thus justifying the higher thrust loss measured for propeller 1 in this test condition. The same physical mechanism was observed in a previous work investigating cruise flight conditions for overlapped propellers [27].

Additionally, comparing the same co-rotating and counter-rotating test cases, the flow topology does not differ significantly until there is an overlapping between the propellers disks. Indeed, the comparison of the flow field at $L_y/R = 1.5$ shows that, for the same disks overlap, the flow acceleration in the propellers slipstream is attenuated for the counter-rotating blades with respect to co-rotating configuration (see Fig. 8(f)). This axial velocity attenuation observed for the counter-rotating case

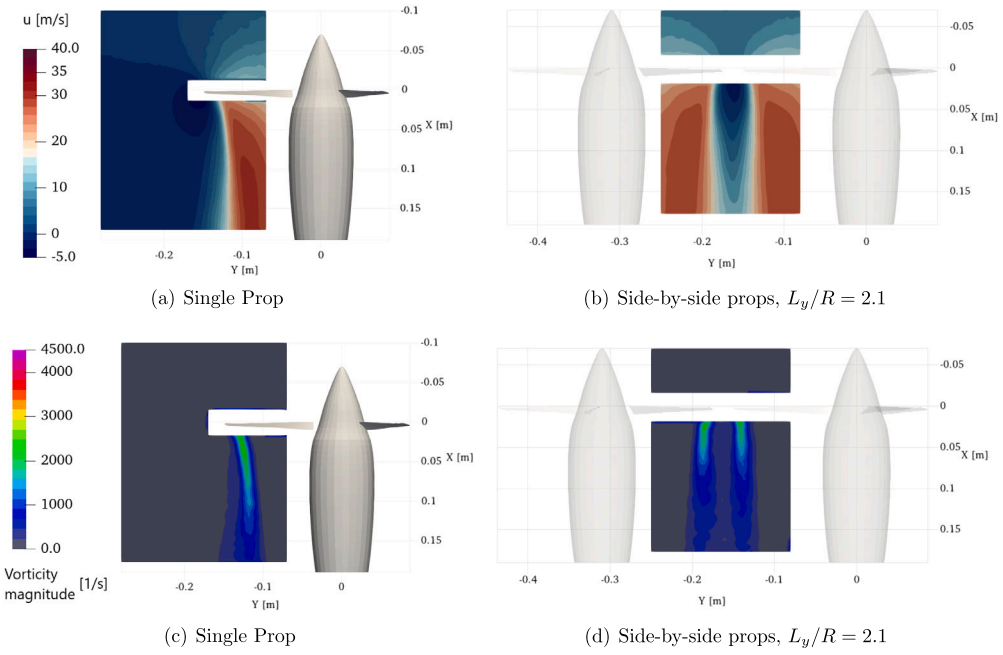

(a) Single Prop (b) Side-by-side props, $L_y/R = 2.1$

(c) Single Prop (d) Side-by-side props, $L_y/R = 2.1$

Fig. 7. Comparison of the ensemble-averaged longitudinal velocity component u contours and vorticity magnitude for the single propeller and side-by-side co-rotating configuration at $L_x = 0$ and $L_y/R = 2.1$.

would provide an opposite effect with respect to the measured performance losses that resulted to be higher than the ones measured for the co-rotating case. Thus, further investigation to explain this effect on performance is provided by the discussion of the flow physics exposed by DUST simulations results in Subsec. 4.1.3, particularly by the analysis of the local angle of attack and sectional loads distributions on rear propeller disk.

Further insights about the $L_x/R = 0.5$ staggered propeller configurations under investigation are given from phase-locked PIV measurements. Fig. 9 shows the comparison of the phase-averaged out-of-plane Z-component vorticity fields for the two configurations with lateral distances $L_y/R = 2$ and $L_y/R = 1.5$ that are characterised by the higher interactional effects. This representation enables to distinguish the vortical structures issued by propeller blades with different sense of rotation (co-rotating and counter-rotating propellers), identified by Z-component vorticity with opposite sign.

In the aligned-tip configuration ($L_y/R = 2$) the vorticity fields between the co-rotating and counter-rotating scenarios are similar, with limited differences occurring only for vortex positions. On the other hand, in the overlapped case $L_y/R = 1.5$, substantial differences occur, as in the co-rotating propellers configurations, the tip vortex structures released by front propeller 2 remain quite coherent in the area of PIV investigation, whereas in the counter-rotating case, these coherent structures are disrupted due to the higher interaction between the two set of vortices released by both propellers blades, thus providing a decrease of the vorticity intensity for the counter-rotating test case. In particular, this different interactional mechanism occurring by changing blades sense of rotation will be discussed in the analysis of numerical simulations results (see Subsec. 4.1.3).

4.1.3. DUST simulations results

A more in-depth analysis is provided in this section for staggered propellers configurations by discussing DUST simulations results, particularly aimed to explain the differences between co-rotating and counter-rotating configurations in relationship with the observed effects on propellers loads. Thus, numerical simulations were performed for the $L_x/R = 0.5$ staggered propeller configurations at two lateral distances $L_y/R = 2$ and $L_y/R = 1.5$ with both co-rotating and counter-rotating blades. Moreover, the single propeller configuration was simulated to provide reference results to evaluate interactional effects.

Firstly, a validation of the numerical model is given by comparison of loads and flow fields with experiments. Fig. 10 shows the comparison between DUST results and measurements of propeller 1 thrust and power coefficients, non-dimensionalised with respect to single propeller values.

Numerical simulations accurately predict the trends of thrust and power losses compared to the experimental data. Indeed, Fig. 10(a) shows that DUST simulations evaluate a maximum thrust loss of about 10% for the overlapped disks configuration accordingly to what observed in the experiment. Moreover, DUST model correctly evaluates the slightly lower thrust loss observed for the co-rotating configuration in the overlapped disks condition compared to the counter-rotating one. Similar considerations can be made for the power coefficient, with a slight overestimation of the power loss evaluated by DUST with respect to experiments.

A further validation of the numerical model is given by the comparison between simulations and PIV surveys in terms of the ensemble-averaged longitudinal velocity component flow fields evaluated for the single propeller and for the co-rotating staggered propellers configurations with $L_y/R = 2$ and $L_y/R = 1.5$. Overall, as can be observed from Fig. 11, the physical phenomenology appears to be accurately captured by DUST in the area of PIV investigation, demonstrating a quite good agreement with experiments for both the lateral distances investigated. In particular, for the single propeller configuration, DUST reproduces accurately the extent of the wake contraction (see Fig. 11(a)). For the staggered test case with $L_y/R = 2$, DUST simulation shows a certain mixing of the two propeller wakes in the lower region of the investigated PIV area as well as provides a slight overestimation of the u velocity values in the propellers interacting wakes with respect to PIV (see Fig. 11(b)). Moreover, a higher propeller 2 wake contraction is noticeable from DUST outcome with respect to experiments for the test case of overlapped propellers (see Fig. 11(c)). This features could be related to the aerodynamic interactions between the propellers, as wake contraction extent is well captured for the single propeller configuration.

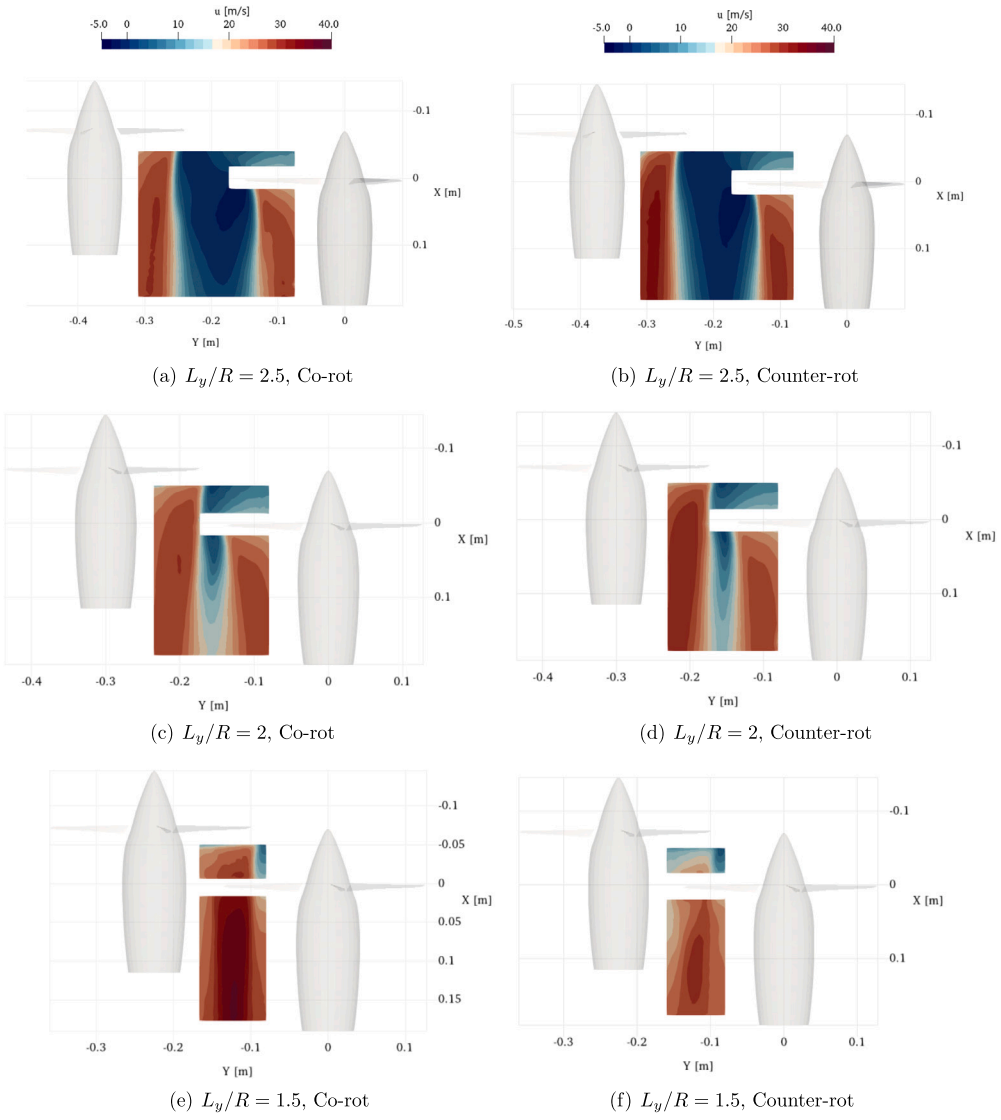

(a) $L_y/R = 2.5$, Co-rot (b) $L_y/R = 2.5$, Counter-rot

(c) $L_y/R = 2$, Co-rot (d) $L_y/R = 2$, Counter-rot

(e) $L_y/R = 1.5$, Co-rot (f) $L_y/R = 1.5$, Counter-rot

Fig. 8. Comparison of the ensemble-averaged longitudinal velocity component u contours for tandem staggered propellers configuration at $L_x/R = 0.5$.

Fig. 12 shows the comparison between the instantaneous phase-averaged out-of-plane Z-component vorticity fields obtained from phase-locked PIV measurements and DUST simulations for the same test cases analysed before. For the investigated test cases the comparison of the vorticity fields shows a quite good agreement in terms of the tip vortex positions with respect to propellers disks. Generally, experimental measurements show a higher vorticity dissipation, while in the numerical results, the vortices remain more coherent at higher distances from propeller disk. This feature is related to natural vorticity dissipation that is slightly differently captured by the simulation also for the single propeller case not affected by aerodynamic interaction (see Fig. 12(a)). On the other hand, for the tandem propellers configurations, vortex sheets resulting from the vorticity released along the span of the propeller blades, which interact with the tip vortices released by both propellers are also accurately represented (see Fig. 12(b)). In particular, for the overlapped disks configuration the deformation of the vortex sheets provided by the interaction with the tip vortices is also well represented by the numerical simulation (see Fig. 12(c)).

The previous comparison of numerical simulations with experimental results in terms of loads and flow fields provided a robust validation of the DUST numerical model. Thus, in the following the numerical solutions are used to provide a more in-depth study of the physical phenomena involved in the analysed staggered propellers configurations. In particular, numerical solutions are used to provide an explanation of the interactional effects between the propellers on the measured loads of propeller 1, particularly considering the blade sense of rotation effect.

Fig. 13 shows a three-dimensional visualization of the numerical flow fields for the staggered propellers configurations obtained by means of Q-Criterion iso-surfaces plotted at blade azimuthal angle $\phi = 0°$. For the aligned-tip configuration ($L_y/R = 2$), the vortical tubes remain coherent until their natural dissipation both for co-rotating and counter-rotating blades (see Figs. 13(a) and 13(c)). On the other hand, in the test case with partial propellers disks overlap, mutual interactions between the vortex structures and between the tip vortices and the blades are apparent. In particular, a different behaviour can be observed in this case between co-rotating and counter-rotating configurations. Indeed, the collision between propeller 1 blades and vortical tubes released by propeller 2 is slightly different as the counter rotation of propeller 2 causes the wake, at the blade level, to be tilted in the opposite direction compared to the co-rotating case (see the region highlighted by red boxes in Figs. 13(b) and 13(d)). A more detailed view of the interactions occurring for the overlapped disk configuration is provided in Fig. 14 by the zoomed view of the three-dimensional iso-contours of Q-criterion captured at three different blade azimuthal

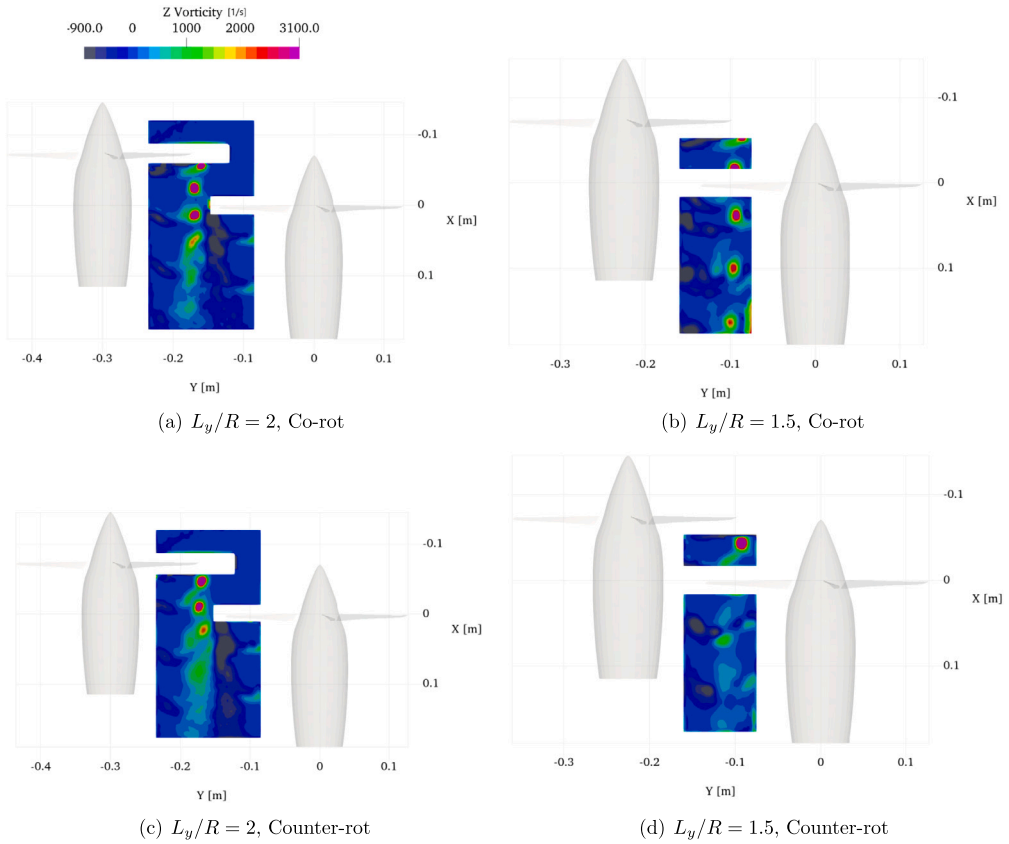

(a) $L_y/R = 2$, Co-rot (b) $L_y/R = 1.5$, Co-rot

(c) $L_y/R = 2$, Counter-rot (d) $L_y/R = 1.5$, Counter-rot

Fig. 9. Comparison of the phase-averaged out-of-plane vorticity Z-component contours for tandem staggered propellers configuration at $L_x = 0.5$ and $\phi = 0°$.

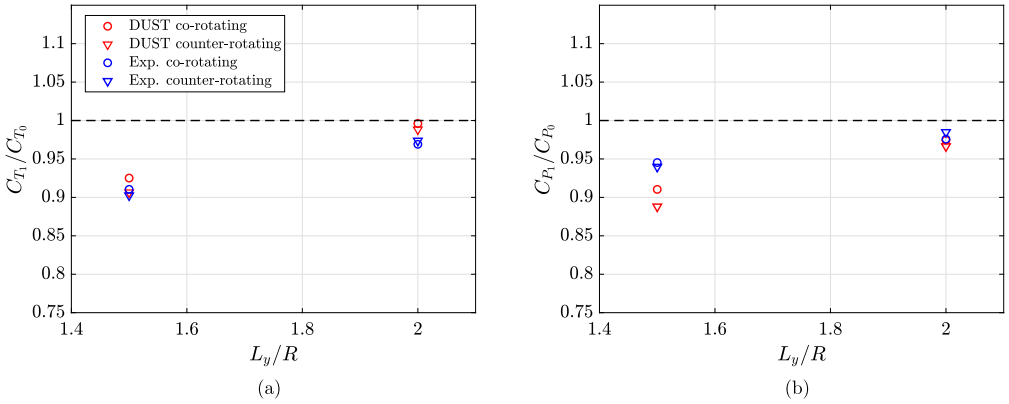

(a) (b)

Fig. 10. Comparison between DUST simulations and experimental results for thrust and power coefficients of propeller 1 in tandem staggered configurations at $L_x = 0.5$.

angles, where blade vortex interaction (BVI) events occur. In particular, the areas of BVI events are highlighted by black boxes.

As can be observed from Fig. 14(a) and 14(d), a first event occurs at $\phi = 90°$ with the collision of propeller 1 blade with a vortex tube released from propeller 2. A second similar event occurs at $\phi = 150°$ (see Fig. 14(b) and 14(e)), while a third event involving a self-collision with a vortex tube released by a previous propeller 1 blade occurs at $\phi = 155°$ (see Fig. 14(c) and 14(f)). The collision events are observed for both co-rotating and counter-rotating test case even if their local flow topology is slightly different, thus providing a different induced velocity field on propeller 1 disk responsible for the variation observed on aerodynamic loading.

This latter effect is supported by the polar plots illustrated in Fig. 15 showing the effective angles of attack and the normal aerodynamic load coefficient experienced by the propeller 1 blade sections throughout the last computed revolution. In particular, the plotted values are subtracted from the corresponding values obtained for the single propeller configuration in order to highlight the interactional effects occurring in tandem configurations. This polar plot analysis is reported for the overlapped disk test configuration only, as for $L_y/R = 2$ the variations of the blade sectional quantities are negligible. A significant drop of the effective angle of attack up to 8° is experienced by propeller 1 blade in the azimuthal angle range between $\phi = 210°$ and $\phi = 270°$. This reduction is limited to about half the propeller radius with the most concentrated reduction in the outer 30% of the blade span. Comparing the polar plots obtained for the two different sense of blade rotation, a lower angle of attack is observed in the counter-rotating case, which justifies the measured lower thrust loading with respect to co-rotating case (see Figs. 15(a) and 15(b)). The negative variation of the effective angle of attack leads to a load loss with respect to single propeller throughout the observed

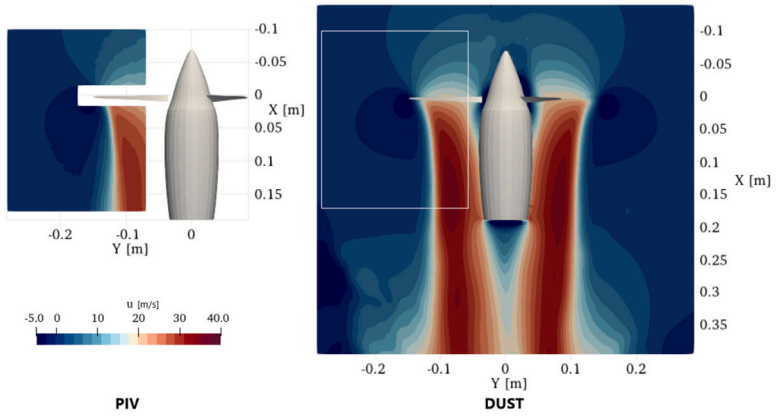

(a) Single Propeller

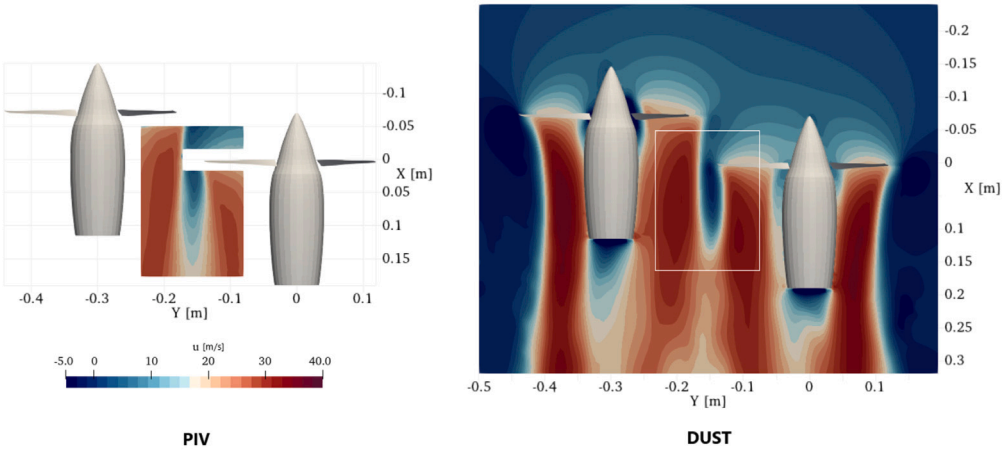

(b) $L_y/R = 2$

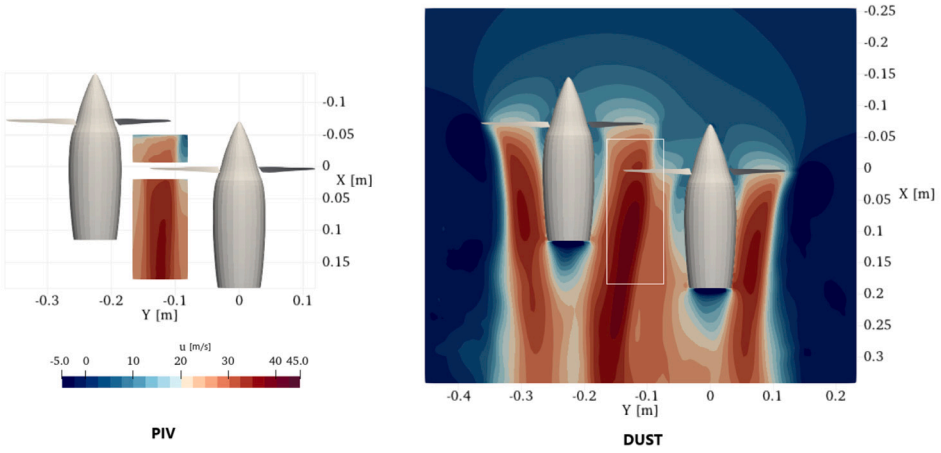

(c) $L_y/R = 1.5$

Fig. 11. Comparison between DUST simulations and PIV results for the ensemble-averaged longitudinal velocity component u contours in single and tandem staggered co-rotating propellers configuration at $L_x/R = 0.5$.

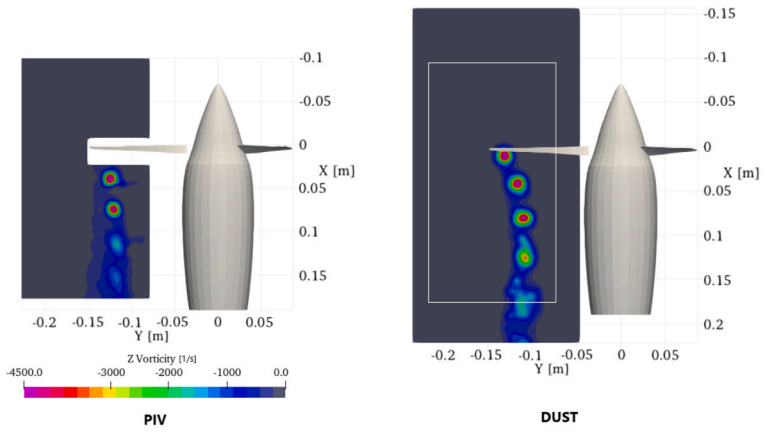

(a) Single Propeller

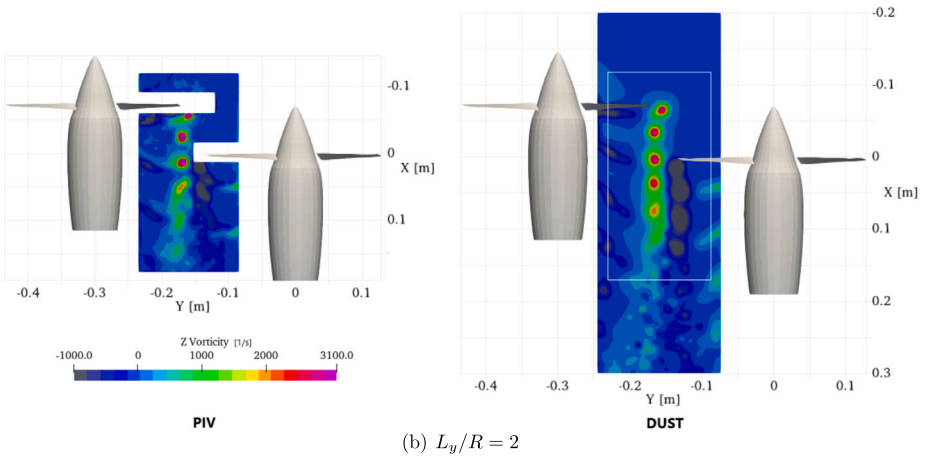

(b) $L_y/R = 2$

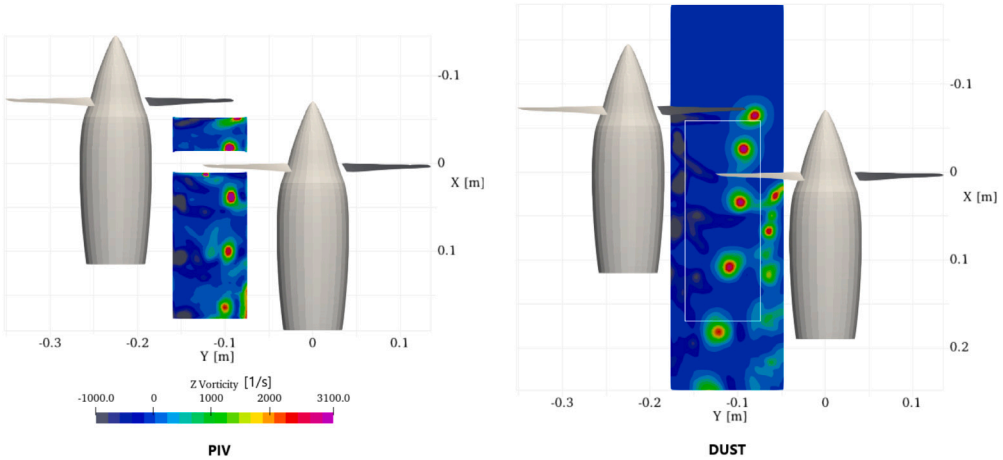

(c) $L_y/R = 1.5$

Fig. 12. Comparison between DUST simulations and PIV results for the phase-averaged out-of-plane Z-component vorticity contours in tandem staggered co-rotating propellers configuration at $L_x/R = 0.5$ and $\phi = 0°$.

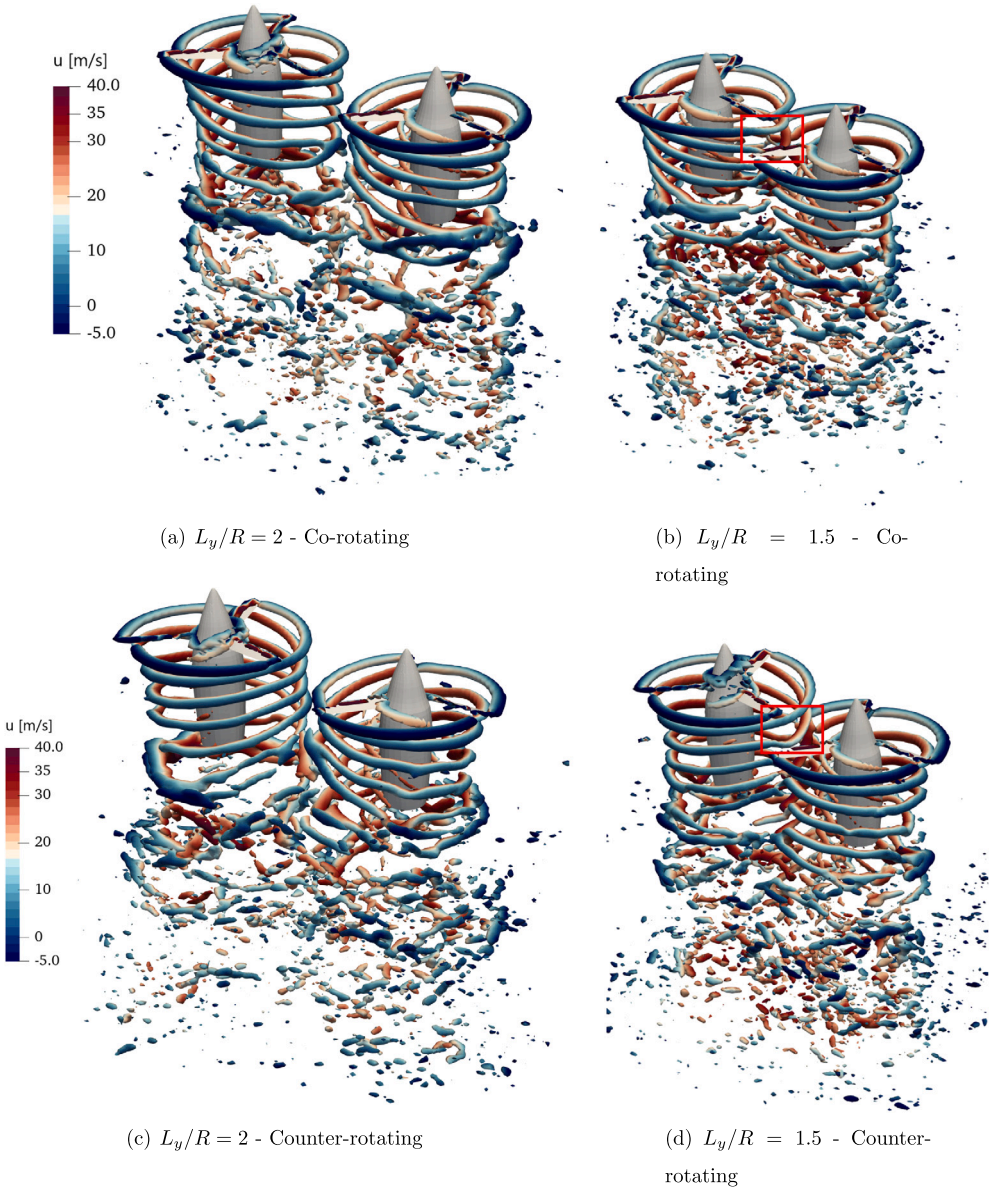

(a) $L_y/R = 2$ - Co-rotating

(b) $L_y/R = 1.5$ - Co-rotating

(c) $L_y/R = 2$ - Counter-rotating

(d) $L_y/R = 1.5$ - Counter-rotating

Fig. 13. Three-dimensional iso-contours of Q-criterion for tandem staggered propellers configurations at $L_x/R = 0.5$ and $\phi = 0°$. Interactional region is highlighted by red boxes. (For interpretation of the colours in the figure(s), the reader is referred to the web version of this article.)

blade azimuthal angle region between $\phi = 210°$ and $\phi = 270°$. Indeed, the lower induced angle of attack evaluated in the counter-rotating case is reflected by the higher reduction of the sectional normal load (see Figs. 15(c) and 15(d)). This representation also shows a positive spike of sectional load at $\phi = 275°$. This spike is related to the third BVI event shown in Fig. 14.

Finally, the time history of the integral thrust coefficient calculated for propeller 1 non-dimensionalized with respect to single propeller values is presented for the overlapped disk test configuration in Fig. 16. A similar periodic behaviour is observed for propeller 1 C_T curves in co-rotating and counter-rotating tandem configurations showing similar events of aerodynamic interaction provided by propeller 2 slipstream impinging on propeller 1 disk. In particular, the first two BVI events analysed in Fig. 14 produce an integral thrust loss up to 20% of the single propeller value in the blade azimuthal angle region between $\phi = 210°$ and $\phi = 270°$. Moreover, the third BVI event occurring at $\phi = 275°$ leads to a positive load spike providing a local impulsive increase of propeller 1 loads with respect to single propeller value. As observed from the sectional load polar plot, the counter-rotating configuration experiences a slightly greater integral thrust loss and a lower positive peak, thus resembling the averaged thrust behaviour measured for this configuration. This periodical behaviour of the propeller loading has a direct influence on acoustic emission, as will be discussed in the following section.

4.2. Acoustic measurements analysis

Acoustic measurements were post-processed from the microphones signals time histories through the analysis of the Power Spectral Density (PSD), the Overall Averaged Sound Pressure Level (OASPL) and the SPL Spectra, which provide information about how the acoustic intensity is distributed across the frequency domain. These quantities are defined as follows:

$$\mathrm{PSD}(f) \equiv \frac{2|X(f)|^2}{T} \quad , \quad X(f) \equiv \int_0^T x(t)\, e^{-2\pi i f t}\, dt \tag{1}$$

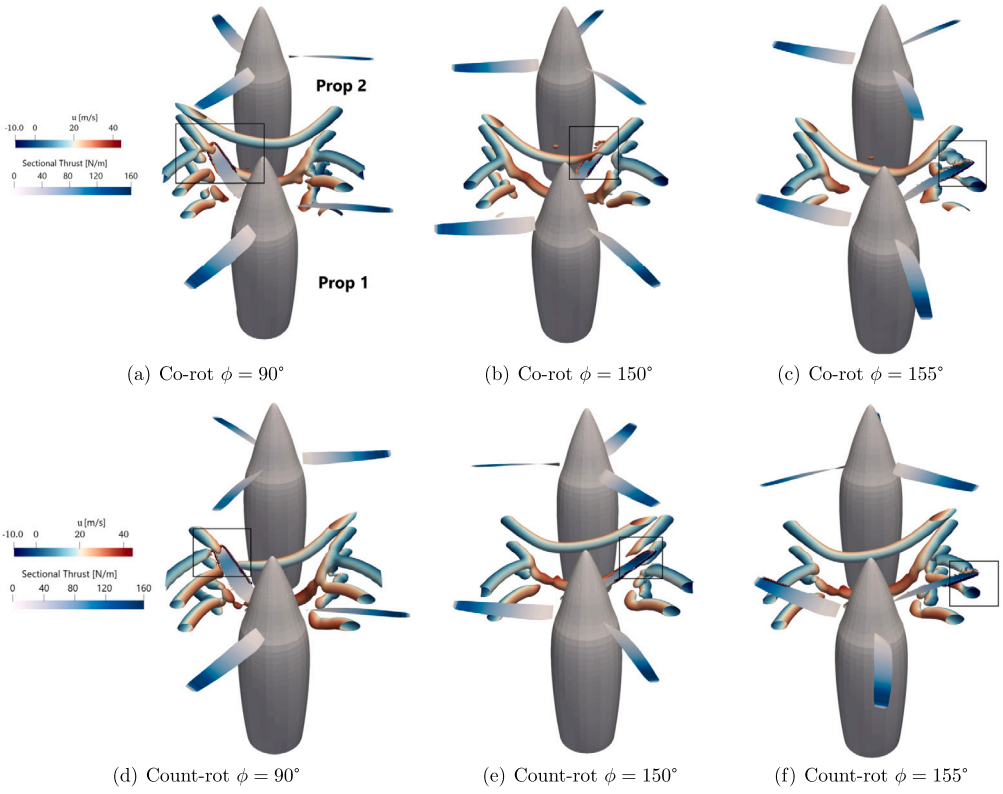

Fig. 14. Particulars of the three-dimensional iso-contours of Q-criterion for tandem staggered propellers configurations at $L_x/R = 0.5$ and different blade azimuthal angles showing BVI events for propeller 1 (highlighted by black boxes).

$$OASPL = 10\log_{10}\left(\frac{\int PSD(f)\,df}{p_{ref}^2}\right) \tag{2}$$

$$SPL\ spectra\ (f) = 10\log_{10}\left(\frac{PSD(f)}{p_{ref}^2}\right) \tag{3}$$

where T is the observation time, 150 Hz $< f <$ 20 kHz and $p_{ref} = 20 * 10^{-6}$ Pa.

In Fig. 17, the acoustic emissions of the investigated propellers in different configurations are compared in terms of the overall averaged sound pressure level (OASPL). The objective is to highlight, as done for the loads and flow fields, the effects of the lateral and longitudinal separation between the propellers as well as the effect of the blade sense of rotation for staggered configurations. Fig. 17(a) shows the acoustic measurements results obtained for side-by-side co-rotating propellers ($L_x/R = 0$) by varying the lateral separation L_y and compared with the acoustic emission of the single propeller. The sound directivity plot of the single propeller showing almost a dipolar behaviour is in agreement with the outcomes of the measurements performed by Zawodny et al. [38] and Celik et al. [21] by using a microphone polar array covering only a partial angular sector around the propeller. It can be observed that the dependence of acoustic emission on lateral separation in the side-by-side case is almost negligible, as the SPL curves of the configurations are almost overlapped. Moreover, an maximum increase of about 10 dB is observed for the acoustic emission of the two side-by-side propellers with respect to the single propeller case. The amount of increase of noise emission obtained for the dual-propeller configuration is in agreement with the outcomes of the measurements performed for a similar set up by Celik et al. [21].

Fig. 17(b) shows the acoustic measurements results obtained for tandem staggered co-rotating propellers with $L_x/R = 0.5$ by varying the lateral separation L_y. A strong dependence on lateral separation can be observed. In particular, the acoustic emission slightly increases by reducing the distance from $L_y/R = 2.5$ to $L_y/R = 2$, due to a limited interaction occurring between propellers wakes as described in flow field analysis. On the other hand, for the condition characterised by partial overlap of the propellers disks ($L_y/R = 1.5$), the SPL distribution increases significantly (about 4 dB in front of the propellers, $\theta = 0°$), as this condition is characterised by a higher degree of aerodynamic interaction between the front propeller slipstream and the rear propeller disk, also providing a robust decrease of propeller 1 aerodynamic performance previously discussed. The increase of the acoustic emission in this case is correlated to the time history of the propeller 1 thrust shown in Fig. 16 characterised by a high amplitude periodic load variation. Moreover, the effect of blade sense of rotation on acoustic emission can be observed for the overlapped propellers disks test case ($L_y/R = 1.5$) in Fig. 17(c). Acoustic measurements show a slightly higher SPL for the counter-rotating propellers case characterised by a higher degree of aerodynamic interaction, as previously discussed in the flow field analysis.

Finally, Fig. 17(d) shows the effect of longitudinal distance (L_x) on acoustic emission by comparing the overall SPL measured for both side-by-side and staggered propellers configurations as a function of L_x at fixed $L_y/R = 2.5$. In particular, for the side-by-side configuration the acoustic measurements show a higher sound emission. Indeed, the higher aerodynamic interaction that occurs when propellers disks are aligned is responsible of an increase of sound that is almost doubled with respect to the variation measured between the two investigated staggered configurations, $L_x/R = 0.5$ and $L_x/R = 1$. This effect is well correlated to the loads measurements showing a higher performance loss for side-by-side configuration at $L_y/R = 2.5$ with respect to the staggered cases (see Fig. 5).

Fig. 18 shows the SPL spectra of the acoustic emissions of the propellers in the isolated propeller case and in the side-by-side configuration with highest interaction, i.e. $L_y/R = 2.1$, measured by three different microphones. In particular, θ represents the azimuthal angle position of the microphones, as shown in Fig. 1. It can be seen that the largest acoustic emission at first BPF is found at $\theta = 90°$, i.e. in the plane

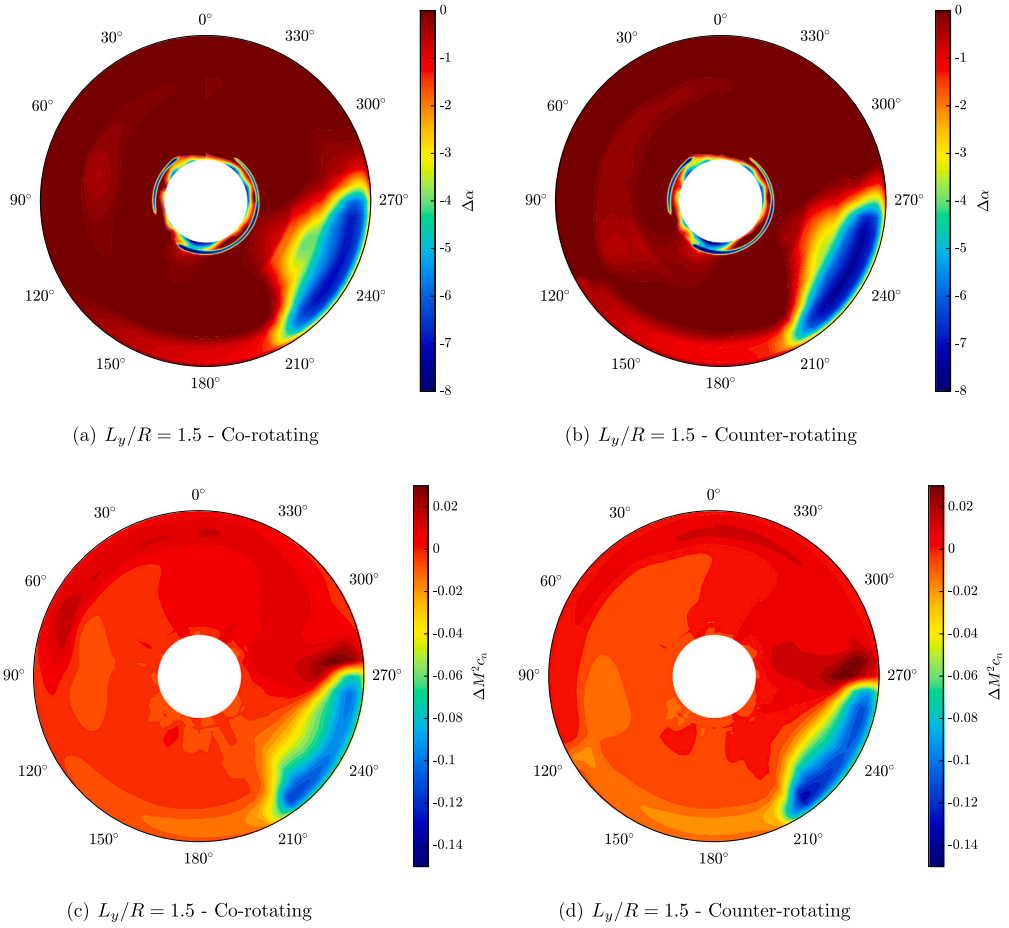

(a) $L_y/R = 1.5$ - Co-rotating

(b) $L_y/R = 1.5$ - Counter-rotating

(c) $L_y/R = 1.5$ - Co-rotating

(d) $L_y/R = 1.5$ - Counter-rotating

Fig. 15. Comparison of the variation of the effective angles of attack $\Delta\alpha$ and of the normal aerodynamic load coefficient $\Delta M^2 c_n$ experienced by the propeller 1 blade sections throughout the last computed revolution with respect to single propeller values, $L_x/R = 0.5$.

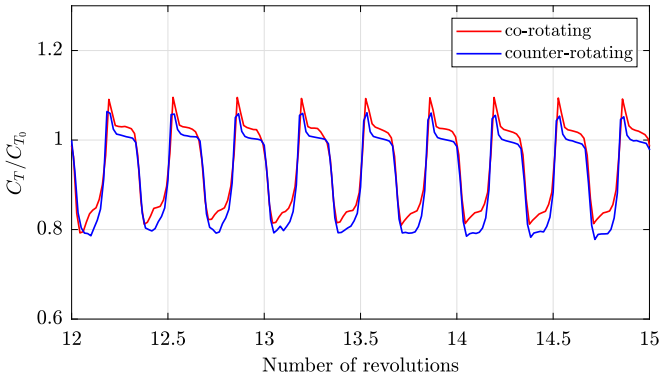

Fig. 16. Comparison of the thrust coefficient time histories calculated by DUST for propeller 1 for the staggered tandem propellers configuration at $L_x/R = 0.5$ and $L_x/R = 1.5$.

of the propellers disk. This can be attributed to a dominant contribution of thickness noise at lowest harmonics. However, for the higher BPFs the largest emissions are found in front of the propellers ($\theta = 0^\circ$). Similar distributions were found for both single and side-by-side propellers configurations, where the latter shows higher peaks due to the dual propellers contribution.

The comparison between the SPL spectra measured by three microphones for the staggered configuration at $L_y/R = 2.5$ and overlapped configuration at $L_y/R = 1.5$ is shown in Fig. 19. For $\theta = 0^\circ$ and $\theta = 180^\circ$, i.e. respectively the front and backward directions with respect to propellers disks, an increase in tonal noise across all BPFs frequencies can be observed for the configuration characterised by overlapped propellers disks. On the other hand, in the in-plane direction $\theta = 90^\circ$, the first two BPFs are not much influenced by the slipstreams interaction related to the overlapping of the propeller disks, while higher BPF frequencies are evenly separated. This can be explained by the fact that BVIs occurring when propellers slipstreams interact mainly influence the loading noise at higher frequencies providing a weak effect on thickness noise at lower frequencies.

The broadband component can also be a huge contributor to noise, in particular when the subject of interest is caught in a turbulent flow. Indeed, in the tandem propeller configuration, propeller 1 is caught in the wake of propeller 2, particularly for overlapped disks configuration. In the staggered configurations blade vortices interact with a solid body thus generating a non-periodic broadband noise that translate into the SPL spectra as low random fluctuations distributed over different frequencies.

To better visualise broadband noise contribution, a least-squares interpolation on the SPL spectrum curve was performed at points between the multiples of the BPF, as similarly done by Zawodny et al. [38] to avoid tonal contributions. This approach isolates the frequency trend caused by tonal frequencies from that of background noise, which is distributed across all frequencies. A comparison between broadband noise spectra measured by three microphones for the staggered configuration at $L_x/R = 0.5$, $L_y/R = 2.5$ and overlapped configuration at $L_x/R = 0.5$, $L_y/R = 1.5$ is shown in Fig. 20. In general, the dual propellers staggered configurations show a quite uniform increment in the broadband noise over all the frequencies with respect to the single propeller case.

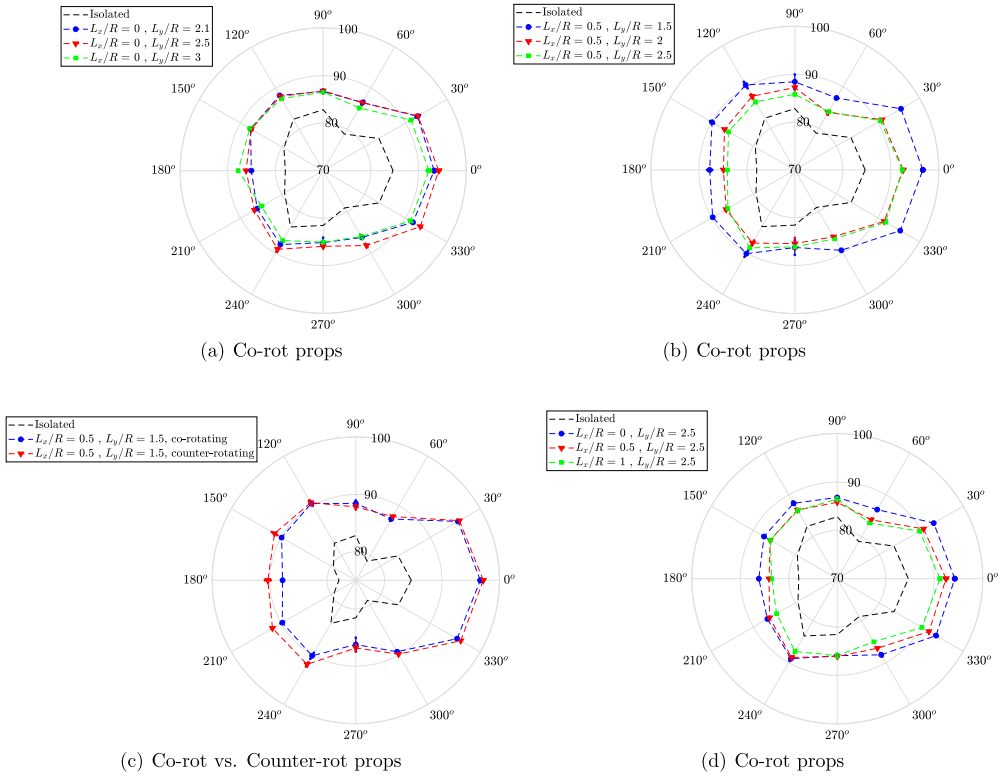

(a) Co-rot props (b) Co-rot props

(c) Co-rot vs. Counter-rot props (d) Co-rot props

Fig. 17. Comparison of the overall averaged SPL, longitudinal distance, lateral distance and sense of blade rotation studies.

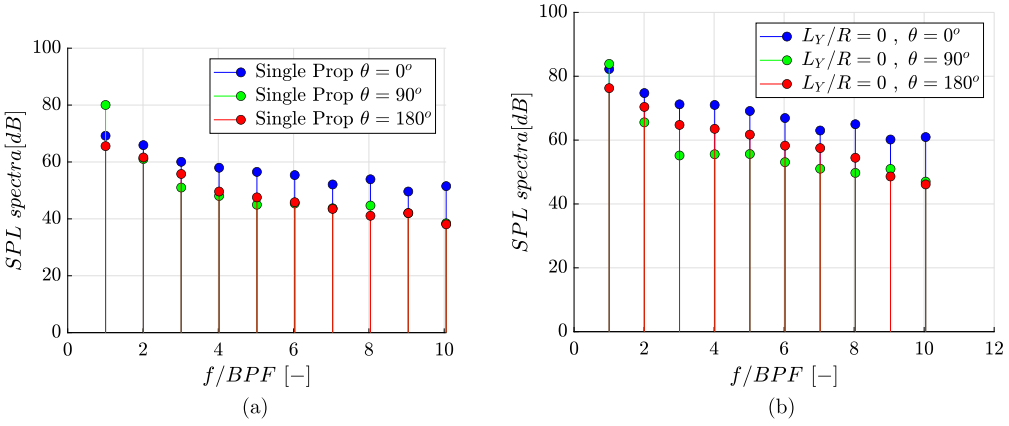

(a) (b)

Fig. 18. Comparison of SPL spectra for co-rotating single propeller and side-by-side configuration at $L_y/R = 2.1$ and different azimuthal positions of microphones.

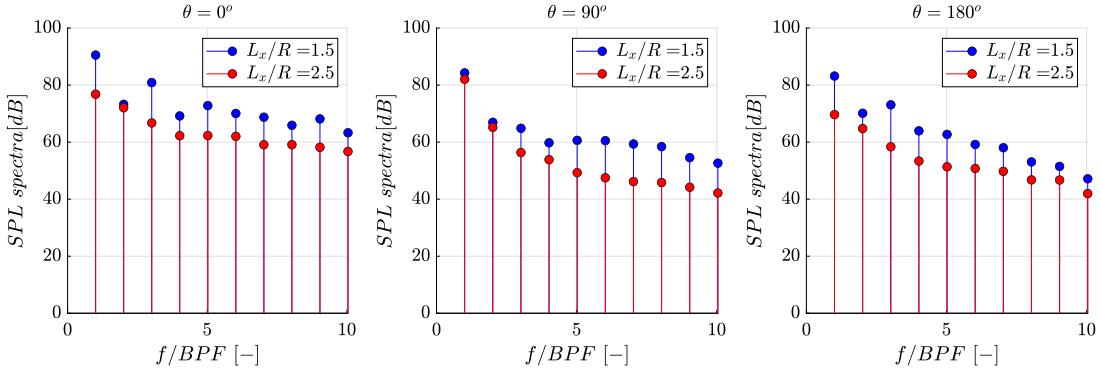

Fig. 19. Comparison of SPL spectra for co-rotating configurations at $L_x/R = 0.5$ and different azimuthal positions of microphones.

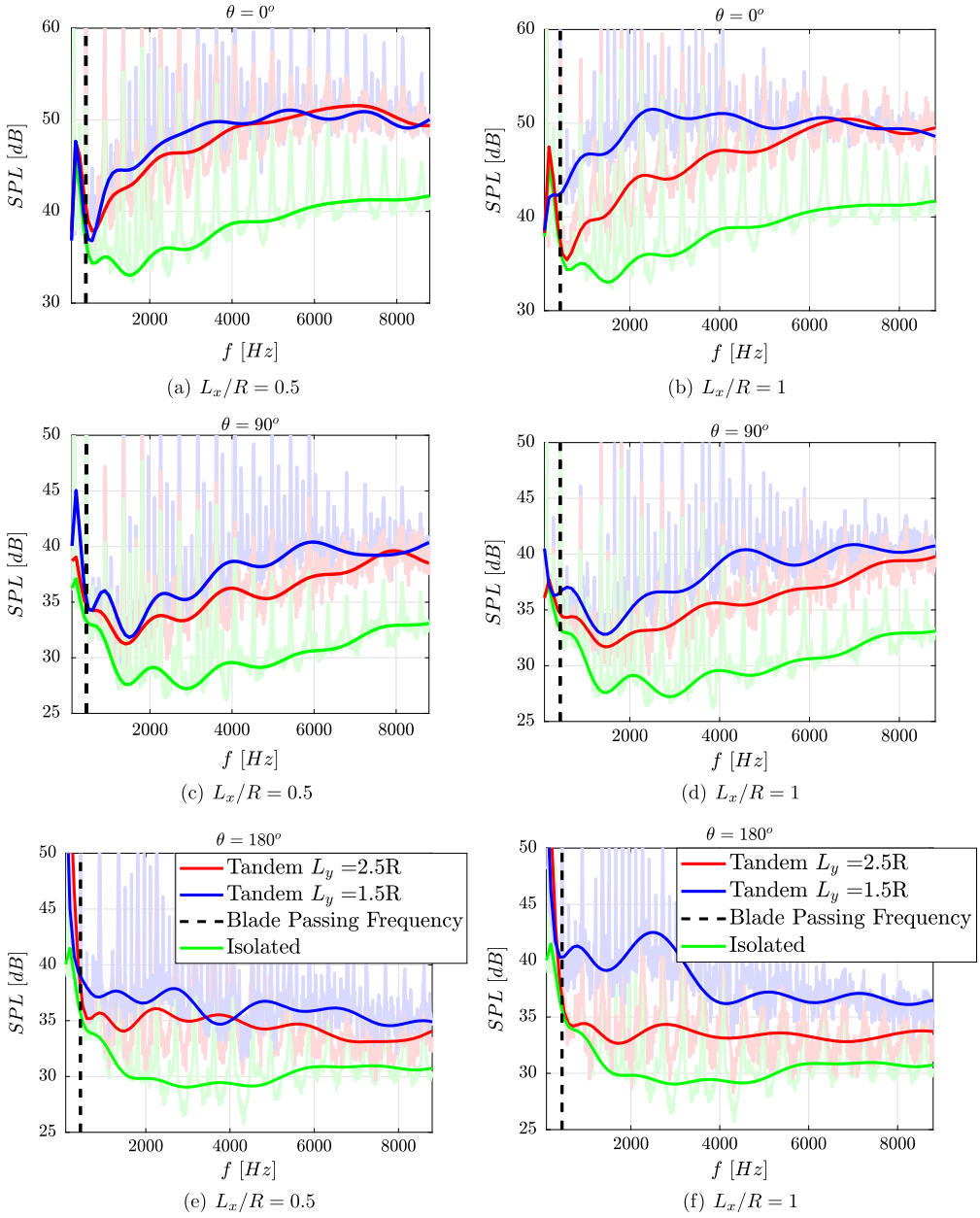

Fig. 20. Comparison of the broadband noise spectra for co-rotating configurations at $L_x/R = 0.5$ and $L_x/R = 1$ and different azimuthal positions of microphones.

In particular, the broadband noise in the staggered configuration shows an higher contribution when the two propellers disks are overlapped ($L_y/R = 1.5$) with respect to the test case with a lateral separation of the propellers ($L_y/R = 1.5$). Similar considerations can be done for $L_x/R = 1$, in Fig. 20, but higher differences can be highlighted with respect to configurations with $L_x/R = 0.5$, probably due to the increased turbulence level characterising the front propeller wake impinging propeller 1 disk for higher longitudinal separations.

5. Conclusions

A comprehensive experimental campaign was performed at Politecnico di Milano aimed to evaluate the interactional effects on aerodynamic performance and noise emission of different tandem propellers configurations in hover. In particular, the test campaign included both side-by-side configurations with propellers disk lying on the same plane and staggered configurations characterised by different longitudinal distances between propellers disks. These latter configurations enabled also to investigate the effects of partial overlap between propellers disks on both aerodynamic performance and aeroacoustics.

Side-by-side propellers results confirmed a slight influence on propellers loading also at very low lateral distance between propellers blades. This slight interactional effect provides also a small variation on acoustic footprint by varying the lateral distance between propellers axis of rotation. A similar trend concerning aerodynamic performance and acoustic emission was found by staggering the propellers disks without overlapping them. On the other hand, a partial overlap between propellers disks provides a robust loss of aerodynamic performance for the propeller invested by front propeller slipstream. Blades sense of rotation effect was investigated particularly for this overlapped configuration, showing that counter-rotating propellers is characterised by a more intense degree of interaction between propellers wakes, supporting the slightly higher performance loss observed for the rear propeller. Moreover, acoustic measurements confirmed an increase of acoustic footprint

for the partial overlapped disk configuration that is almost two times greater than the one observed by changing the lateral distance between the propellers without disk overlap.

Generally speaking, the analysis of the main results presented in this work enabled to correlate the effect of the aerodynamic interaction between the propellers on aerodynamic performance with noise emission, particularly exploring novel test configurations with respect to recent literature.

CRediT authorship contribution statement

Daniele Granata: Writing – original draft, Visualization, Validation, Software, Methodology, Investigation, Formal analysis, Data curation, Conceptualization. **Alberto Savino:** Visualization, Validation, Software, Methodology, Investigation, Data curation, Conceptualization. **Donato Grassi:** Validation, Supervision, Methodology, Investigation, Conceptualization. **Luca Riccobene:** Validation, Supervision, Methodology, Investigation, Formal analysis, Conceptualization. **Alex Zanotti:** Writing – review & editing, Writing – original draft, Validation, Supervision, Resources, Project administration, Methodology, Investigation, Funding acquisition, Data curation, Conceptualization.

Declaration of competing interest

The authors declare that they have no known competing financial interests or personal relationships that could have appeared to influence the work reported in this paper.

Acknowledgements

The research leading to the presented results has been addressed within the framework of the HC/AG-26 “Noise Radiation and Propagation for Multirotor System Configurations”, supported by GARTEUR. This research was performed by using staff, instrumentation and facilities of Politecnico di Milano. Model manufacturing was funded by basic research funding of Politecnico di Milano. Authors would like to acknowledge Roberto Fugamalli for his support in the acoustic measurements.

Data availability

Data will be made available on request.

References

[1] N. Polaczyk, E. Trombino, P. Wei, M. Mitici, A review of current technology and research in urban on-demand air mobility applications, in: 8th Biennial Autonomous VTOL Technical Meeting and 6th Annual Electric VTOL Symposium, Vertical Flight Soc. Mea, Arizona, 2019, pp. 333–343.

[2] M. Wentrup, J. Yin, P. Kunze, T. Streit, J.-H. Wendisch, T. Schwarz, J.-P. Pinacho, K. Kicker, R. Fukari, An overview of dlr compound rotorcraft aerodynamics and aeroacoustics activities within the cleansky2 nacor project, in: AHS Forum 2018, 2018.

[3] S.A. Tran, J.W. Lim, Interactional aerodynamics of the xv-15 tiltrotor aircraft during conversion maneuvers, J. Am. Helicopter Soc. 67 (3) (2022) 56–68.

[4] J.F. Tan, T.Y. Zhou, Y.M. Sun, G.N. Barakos, Numerical investigation of the aerodynamic interaction between a tiltrotor and a tandem rotor during shipboard operations, Aerosp. Sci. Technol. 87 (2019) 62–72.

[5] S. Tran, J. Lim, G. Nunez, A. Wissink, G. Bowen-Davies, Cfd calculations of the xv-15 tiltrotor during transition, in: Proceedings of the American Helicopter Society 75th Annual Forum, Philadelphia, PA, USA, 2019, pp. 13–16.

[6] R. de Vries, N. van Arnhem, T. Sinnige, R. Vos, L.L. Veldhuis, Aerodynamic interaction between propellers of a distributed-propulsion system in forward flight, Aerosp. Sci. Technol. 118 (2021) 107009.

[7] G. Droandi, A. Zanotti, G. Gibertini, Aerodynamic interaction between rotor and tilting wing in hovering flight condition, J. Am. Helicopter Soc. 60 (4) (2015) 1–20.

[8] G. Droandi, M. Syal, G. Bower, Tiltwing multi-rotor aerodynamic modeling in hover, transition and cruise flight conditions, in: AHS International 74th Annual Forum & Technology Display, vol. 1, AHS International, Fairfax, VA, 2018, pp. 46–62.

[9] D. Montagnani, M. Tugnoli, A. Zanotti, M. Syal, G. Droandi, et al., Analysis of the interactional aerodynamics of the vahana evtol using a medium fidelity open source tool, in: VFS Aeromechanics for Advanced Vertical Flight Technical Meeting, Vertical Flight Society, 2020, pp. 436–451.

[10] R. Piccinini, M. Tugnoli, A. Zanotti, Numerical investigation of the rotor-rotor aerodynamic interaction for evtol aircraft configurations, Energies 13 (22) (2020) 5995.

[11] D. Opoku, D. Triantos, F. Nitzsche, S. Voutsinas, Rotorcraft aerodynamic and aeroacoustic modelling using vortex particle methods, in: Proceedings of the 23rd International Congress of Aeronautical Sciences, ICAS, Toronto, Canada, 2002.

[12] T. Su, Y. Lu, J. Ma, S. Guan, Aerodynamic characteristics analysis of electrically controlled rotor based on viscous vortex particle method, Aerosp. Sci. Technol. 97 (2020) 105645.

[13] C. Sheng, J.C. Narramore, Computational simulation and analysis of bell boeing quad tiltrotor aero interaction, J. Am. Helicopter Soc. 54 (4) (2009) 42002.

[14] Z. Jia, S. Lee, Acoustic analysis of a quadrotor evtol design via high-fidelity simulations, in: 25th AIAA/CEAS Aeroacoustics Conference, 2019.

[15] A. Zarri, E. Dell’Erba, W. Munters, C. Schram, Aeroacoustic installation effects in multi-rotorcraft: numerical investigations of a small-size drone model, Aerosp. Sci. Technol. 128 (2022) 107762, https://doi.org/10.1016/j.ast.2022.107762, https://www.sciencedirect.com/science/article/pii/S1270963822004369.

[16] J. Sagaga, S. Lee, High-fidelity computational study of aerodynamic noise of side-by-side rotor in full configuration, J. Sound Vib. 592 (2024) 118607, https://doi.org/10.1016/j.jsv.2024.118607, https://www.sciencedirect.com/science/article/pii/S0022460X24003705.

[17] A.D. Thai, E. De Paola, A. Di Marco, L.G. Stoica, R. Camussi, R. Tron, S.M. Grace, Experimental and computational aeroacoustic investigation of small rotor interactions in hover, Appl. Sci. 11 (21) (2021).

[18] C. Poggi, G. Bernardini, M. Gennaretti, R. Camussi, Scalability of mach number effects on noise emitted by side-by-side propellers, Appl. Sci. 12 (19) (2022), https://www.mdpi.com/2076-3417/12/19/9507.

[19] S.O. Afari, R.R. Mankbadi, Simulations of multi-rotor interaction noise at hovering & forward flight conditions, Int. J. Aeroacoust. 22 (1–2) (2023) 153–187.

[20] E.J. Alvarez, A. Schenk, T. Critchfield, A. Ning, Rotor-on-rotor aeroacoustic interactions of multirotor in hover, in: Proceedings of the Vertical Flight Society’s 76th Annual Forum & Technology Display, Virtual, 2020.

[21] A. Celik, N. Syafiqah Jamaluddin, K. Baskaran, S. Meloni, D. Rezgui, M. Azarpeyvand, Experimental characterisation of rotor noise in tandem configuration, Appl. Acoust. 222 (2024) 110053, https://doi.org/10.1016/j.apacoust.2024.110053, https://www.sciencedirect.com/science/article/pii/S0003682X24002044.

[22] R.E. Nargi, P. Candeloro, F. De Gregorio, G. Ceglia, T. Pagliaroli, Fluid-dynamic and aeroacoustic characterization of side-by-side rotor interaction, Aerospace 10 (10) (2023).

[23] N.S. Zawodny, D.D. Boyd, D.M. Nark, Aerodynamic and acoustic interactions associated with inboard propeller-wing configurations, in: AIAA Scitech 2021 Forum, 2021, p. 0714.

[24] J. Goldschmidt, H. Tingle, P. Ifju, S.A. Miller, L.S. Ukeiley, B. Goldman, G. Droandi, K. Lee, Acoustics and forces from isolated and installed tandem evtol rotor configurations, in: AIAA SCITECH 2023 Forum, 2023, p. 0791.

[25] F.d. Monteiro, R. Duivenvoorden, D. Ragni, F. Avallone, T. Sinnige, Experimental analysis of synchrophasing impact on noise of distributed propeller systems in tractor configuration, in: 30th AIAA/CEAS Aeroacoustics Conference 2024, 2024, p. 3421.

[26] J. Yin, K.-S. Rossignol, L. Rottmann, T. Schwarz, Numerical investigations on small-scale rotor configurations with validation using acoustic wind tunnel data, in: 48th European Rotorcraft Forum, 2022.

[27] A. Zanotti, D. Algarotti, Aerodynamic interaction between tandem overlapping propellers in evtol airplane mode flight condition, Aerosp. Sci. Technol. 124 (2022) 107518.

[28] A. Zanotti, A. Velo, C. Pepe, A. Savino, D. Grassi, L. Riccobene, Aerodynamic interaction between tandem propellers in evtol transition flight configurations, Aerosp. Sci. Technol. (2024) 109017.

[29] A. Zanotti, L. Menini, A. Savino, D. Grassi, L. Riccobene, Experimental investigation of wing-propeller aerodynamic interaction in evtol configurations, Aerosp. Sci. Technol. 152 (2024) 109348, https://doi.org/10.1016/j.ast.2024.109348, https://www.sciencedirect.com/science/article/pii/S1270963824004796.

[30] C. Niro, A. Savino, A. Cocco, A. Zanotti, Mid-fidelity numerical approach for the investigation of wing-propeller aerodynamic interaction, Aerosp. Sci. Technol. (2024) 108950.

[31] M. Tugnoli, D. Montagnani, M. Syal, G. Droandi, A. Zanotti, Mid-fidelity approach to aerodynamic simulations of unconventional vtol aircraft configurations, Aerosp. Sci. Technol. 115 (2021) 106804.

[32] D. Weitsman, J.H. Stephenson, N.S. Zawodny, Effects of flow recirculation on acoustic and dynamic measurements of rotary-wing systems operating in closed anechoic chambers, J. Acoust. Soc. Am. 148 (3) (2020) 1325–1336.

[33] J.H. Stephenson, D. Weitsman, N.S. Zawodny, Effects of flow recirculation on unmanned aircraft system (uas) acoustic measurements in closed anechoic chambers, J. Acoust. Soc. Am. 145 (3) (2019) 1153–1155.

[34] G.S. Winckelmans, Topics in Vortex Methods for the Computation of Three-and Two-Dimensional Incompressible Unsteady Flows, California Institute of Technology, 1989.

[35] D. Montagnani, M. Tugnoli, F. Fonte, A. Zanotti, M. Syal, G. Droandi, et al., Mid-fidelity analysis of unsteady interactional aerodynamics of complex vtol configurations, in: 45th European Rotorcraft Forum (ERF 2019), 2019, pp. 100–110.

[36] C. Pepe, A. Velo, Experimental and numerical investigation of aerodynamic interaction between tandem propellers in conversion manoeuvre, Master's thesis, Politecnico di Milano, 2023.

[37] W. Zhou, Z. Ning, H. Li, H. Hu, An experimental investigation on rotor-to-rotor interactions of small uav propellers, in: 35th AIAA Applied Aerodynamics Conference, 2017, p. 3744.

[38] N.S. Zawodny, D.D. Boyd Jr, C.L. Burley, Acoustic characterization and prediction of representative, small-scale rotary-wing unmanned aircraft system components, in: American Helicopter Society (AHS) Annual Forum, no. NF1676L-22587, 2016.